Ratios of maximal concurrence-parameterized separability functions, and generalized Peres–Horodecki conditions

2009 J. Phys. A: Math. Theor. 42 465305

(http://iopscience.iop.org/1751-8121/42/46/465305)

IOP PUBLISHING JOURNAL OF PHYSICS A: MATHEMATICAL AND THEORETICAL

J. Phys. A: Math. Theor. **42** (2009) 465305 (33pp) doi:10.1088/1751-8113/42/46/465305

Ratios of maximal concurrence-parameterized separability functions, and generalized Peres–Horodecki conditions

Paul B Slater

ISBER, University of California, Santa Barbara, CA 93106, USA

E-mail: slater@kitp.ucsb.edu

Received 13 July 2009, in final form 8 September 2009
Published 22 October 2009
Online at stacks.iop.org/JPhysA/42/465305

Abstract

The probability that a generic real, complex or quaternionic two-qubit state is separable can be considered to be the sum of three contributions. One is from those states that are *absolutely* separable, that is those (which can not be entangled by unitary transformations) for which the *maximal concurrence* over spectral orbits ($C_{\max}$) is zero. The other two contributions are from the states for which $C_{\max} \in \left(0, \frac{1}{2}\right]$, and for which $C_{\max} \in \left[\frac{1}{2}, 1\right]$. We have previously (arXiv:0805.0267) found exact formulas for the absolutely separable contributions in terms of the Hilbert–Schmidt metric over the quantum states, and here advance hypotheses as to the exact contributions for $C_{\max} \in \left[\frac{1}{2}, 1\right]$. A crucial element in understanding the two contributions for $C_{\max} > 0$ is the nature of the ratio (R) of the $C_{\max}$-parameterized separability function for the complex states to the *square* of the comparable function for the real states–both such functions having clearly displayed jump discontinuities at $C_{\max} = \frac{1}{2}$. For $C_{\max} \in \left(0, \frac{1}{2}\right]$, the ratio R appears to be of the form $1 + kC_{\max}$, except near $C_{\max} = \frac{1}{2}$, while for $C_{\max} \in \left[\frac{1}{2}, 1\right]$, there is strong numerical evidence that it equals 2 (thus, according to the Dyson-index pattern of random matrix theory). Related phenomena also occur for the minimally degenerate two-qubit states and the qubit–qutrit states. Our results have immediate application to the computation of separability probabilities in terms of other metrics, such as the Bures (minimal monotone) metric. The paper begins with continuous embeddings of the separability probability question in terms of four metrics of interest, using 'generalized Peres–Horodecki conditions'.

PACS numbers: 03.67.Mn, 02.30.Cj, 02.40.Ky, 02.40.Ft

(Some figures in this article are in colour only in the electronic version)

1. Introduction

One possibly productive strategy to pursue when confronted with an apparently intractable problem is to embed it in some broader class of problems. Doing so, hopefully, may lead to new insights and progress, including ones regarding the original (smaller) problem. In the first of the two basic parts of this paper (sections 2–7), we adopt such embedding strategies for the task of determining the probabilities–with regard to a number of metrics of quantum-mechanical interest–that certain generic forms of 2×2 or 2×3 quantum system are separable [1–8]. (As computers presumably grow more powerful, these readily formulated, but high-dimensional (9, 15, etc), and high-degree (e.g. quartic) problems may eventually lose their apparent present-day intractability (cf [9, 10])—much as did the famous four-color planar map theorem of Appel and Haken [11, 12]. Nevertheless, it would certainly be appealing to address these problems with more theoretical understanding than is required by 'brute force' computation (cf [13–16]).)

In the second basic part (sections 8–10), building upon our recent work in [17], we attempt to gain insight—using manifest relations to random matrix theory–into the very same separability probability questions by determining the nature of certain eigenvalue-parameterized separability functions. These are expressed as univariate functions of the maximal concurrence over spectral orbits.

The fundamental question being addressed here of determining the probability that a generic bipartite quantum state is separable or not was first raised by Życzkowski, Horodecki, Sanpera and Lewenstein in a pioneering, much-cited 1998 paper [1]. As motivation they wrote: 'One of the fundamental questions concerning these subjects is to estimate how many entangled (disentangled) states exist among all quantum states. More precisely, one can consider the problem of quantum separability or inseparability from a measurement theoretical point of view, and ask about relative volumes of both sets. There are three main reasons of importance in this problem. The first reason, of some philosophical implication, may be contained in the questions: is the world more classical or more quantum? Does it contain more quantum-correlated (entangled) states than classically correlated ones? The second reason has a more practical origin. Analyzing some features of entanglement, one often has to rely on numerical simulations. It is then important to know to what extent entangled quantum states may be considered as typical. Finally, the third reason has a physical origin. The physical meaning of separability has recently been associated with the possibility of partial time reversal' [1, p 883].

In section 2, in the first basic part of the paper, we analyze the cases of generic 9-dimensional real and 15-dimensional complex two-qubit systems. For our calculations, we utilize the Euler-angle parameterizations of the real (developed by Cacciatori [8, appendix A]) and of the complex 4×4 density matrices (ρ) [18], as well as the Tezuka–Faure (TF) procedure [19, 20] for generating low-discrepancy sets of (9- and 15-dimensional) points. These points are employed for quasi-Monte Carlo numerical integration with respect to the *product* of the (6- or 12-dimensional) Haar measure over the Euler angles and (3-dimensional) metric-specific measures over the eigenvalues of the density matrices. In section 3, we turn our attention to parallel 'continuous embedding' analyses pertaining to the 14-dimensional (rank-3) boundary of the 15-dimensional generic complex 4×4 density matrices.

In section 4, we make use of the $SU(6)$-based Euler-angle parameterization of the 35-dimensional generic complex qubit–*qutrit* 6×6 density matrices [21, section 11] to investigate the corresponding rank-6 and rank-5 problems. In section 5, we investigate formally extending the range of our basic parameter (α)—used in forming convex combinations—from beyond $[0, 1]$ to $[-\infty, \infty]$. In section 6, we depart from our initial paradigm, employing the parameter

α, and evaluate the separability probabilities of the generic complex and real two-qubit states for which the entanglement measure *concurrence* (C) [22, 23] is less than some threshold. (There we observe some interesting behavior, involving the *intersection* of the curves for different metrics. For $C = 1$, we obtain the usual separability probabilities.)

The concept of *maximal* concurrence ($C_{\max}$) over spectral orbits [24]:

$$C_{\max} = \max(0, \lambda_1 - \lambda_3 - 2\sqrt{\lambda_2\lambda_4}), \qquad (\lambda_1 \geqslant \lambda_2 \geqslant \lambda_3 \geqslant \lambda_4) \tag{1}$$

(a quantity which can not be increased under unitary transformations) of a two-qubit density matrix (ρ), where the λ's are the ordered eigenvalues of ρ, is used in the second basic set of analyses of the paper (section 8). There, we importantly add to certain findings [17] concerning the strong goodness-of-fit to two-qubit eigenvalue-parameterized separability functions (ESFs) of piecewise functions of $C_{\max}$. We find evidence of adherence over a *half*-domain $C_{\max} \in \left[\frac{1}{2}, 1\right]$ to a Dyson-index pattern *both* for the generic rank-4 (first investigated in [17]) and generic rank-3 (as found here (section 8.5.1)) real and complex two-qubit states. We, further, undertake an analogous examination of: (a) the generic rank-5 qubit–qutrit states in section 8.6, observing interesting jump discontinuities in the ESFs; and (b) the generic full rank qubit–qutrit states in section 8.7, where, again, the Dyson-index pattern appears to emerge over a restricted domain $C_{\max} \in \left[\frac{1}{3}, 1\right]$. Additionally, in section 9.1, we are able to present new simple exact results pertaining to certain components of the desired Hilbert–Schmidt separability probabilities. In these regards, let us draw the reader's attention, particularly, to (the titular) figures 34 and 35.

Since when we had earlier addressed the issue of two-qubit separability probabilities in terms of *diagonal-entry*-parameterized separability functions (DESFs) [7], we found apparently *total* agreement with Dyson-index behavior, the need (remaining unmet) to reconcile these two forms of Dyson-index patterns (full and partial) is obvious.

Remarks relevant to the two primary sets of analyses—which share the use of concurrence and are devoted to the determination of separability *probabilities*-–are given in sections 7 and 10.

1.1. Separability functions

Let us state here that the concept of a *separability function*-–both in its eigenvalue-parameterized (ESF) and diagonal-entry-parameterized (DESF) forms—has been developed in order to reduce the intrinsically high dimensionalities of the generic separability probability questions. By integrating over the majority of parameters—for example, Euler angles or off-diagonal entries—one reduces the problems (at least, in the two-qubit case) to ones of (only!) a 3-dimensional nature. It also appears possible to further reduce the 3-dimensional problems to single-dimensional ones by finding an appropriate parameter—known to be the ratio of the product of the 11- and 44-diagonal entries to the product of the 22- and 33-diagonal entries in the DESF case, and apparently (as numerics strongly indicate) the maximal concurrence over spectral orbits in the ESF case.

1.2. Metrics employed

The metrics of quantum-mechanical interest that we utilize to form (via their Riemannian volume elements) measures over the quantum systems are the (Euclidean or flat, non-monotone [25]) Hilbert–Schmidt [13] and three monotone metrics [26]—the (minimal monotone) Bures [14], Wigner–Yanase [27] and Kubo–Mori [28] metrics. (We also attempted to include the information-theoretically significant monotone 'quasi-Bures' (Grosse–Krattenthaler–Slater)

metric [5, 29, 30], which yields the minimax/maximin asymptotic redundancy for universal quantum coding, but encountered some initial, at least, numerical difficulties in this regard.)

1.3. Prior conjectures

In [7], we were led by a combination of numerical and theoretical (Dyson-index-related) arguments, involving *diagonal-entry*-parameterized separability functions (DESFs), to conjecture that the Hilbert–Schmidt separability probabilities are, respectively, $\frac{8}{33} \approx 0.242\,424$ for the generic complex two-qubit systems and $\frac{8}{17} \approx 0.470\,588$ for its real counterpart. (The supporting evidence appeared particularly strong for the $\frac{8}{33}$ figure.) Also, it has been further conjectured that for the generic *quaternionic* two-qubit systems, the corresponding probability is $\frac{72\,442\,944}{936\,239\,725} \approx 0.073\,3389$ [31, equation (15)] [8, p 25]).

We had also earlier advanced in [4, table VI], the 'silver mean' (that is, $\sqrt{2}-1$) conjectures that the generic complex two-qubit *Bures* separability probability is

$$P_{sep/Bures}^{\text{complex}} = \frac{1680(\sqrt{2}-1)}{\pi^8} \approx 0.073\,3389 \tag{2}$$

and the corresponding Kubo–Mori analogue is

$$P_{sep/KM}^{\text{complex}} = \frac{1575(\sqrt{2}-1)}{2\pi^8} \approx 0.035\,398. \tag{3}$$

(Additionally, for the 'average monotone metric'—not employed in this paper—it was conjectured in [4] that the associated separability probability is $\frac{81\,664(\sqrt{2}-1)}{75\pi^8} \approx 0.047\,5329$. Further still, the Wigner–Yanase separability probability was hypothesized to equal the ratio of $\frac{7(\sqrt{2}-1)}{4}$ to the not-yet-determined Wigner–Yanase volume of the generic (entangled and separable) complex two-qubit states.)

In [7, section 10], again studying the corresponding DESFs, the conjectures were put forth that the generic real and complex qubit–*qutrit* Hilbert–Schmidt separability probabilities are $\frac{32}{213} \approx 0.150\,235$ and (agreeing very closely with the numerics) $\frac{32}{1199} \approx 0.026\,6889$, respectively.

2. Generic full-rank real and complex two-qubit cases

2.1. First set of constraints—convex combinations of determinants of ρ and ρ_{PT}

2.1.1. Real two-qubit density matrices. In figure 1, we show as a function of $\alpha \in [0, 1]$ the probabilities $\left(P_{\text{metric}}^{\text{real}}(\alpha)\right)$, in terms of the four metrics under consideration, that for a generic (9-dimensional) real two-qubit system,

$$\alpha|\rho_{PT}| + (1-\alpha)|\rho| \geqslant 0. \tag{4}$$

Here ρ_{PT} is the partial transpose of ρ and $|\rho_{PT}|$, its determinant. Of course, here and throughout we incorporate into our analyses, the original, notable Peres–Horodecki necessary and sufficient conditions for separability in terms of the nonnegativity of ρ_{PT} [32, 33]. The partial transpose of a 4×4 density matrix can have at most one negative eigenvalue, so the condition $|\rho_{PT}| < 0$ is fully equivalent to ρ_{PT} having a single negative eigenvalue [34]. (Also, obviously, the nonnegativity condition $|\rho| \geqslant 0$ is always satisfied.)

The order of dominance of the four monotonically decreasing curves in figure 1, as well as all the other analogous curves below, turns out—with the important exception of those in section 6.2, where we observe *intersecting* behavior—to be

$$\text{Hilbert–Schmidt} > \text{Bures} > \text{Wigner–Yanase} > \text{Kubo–Mori}. \tag{5}$$

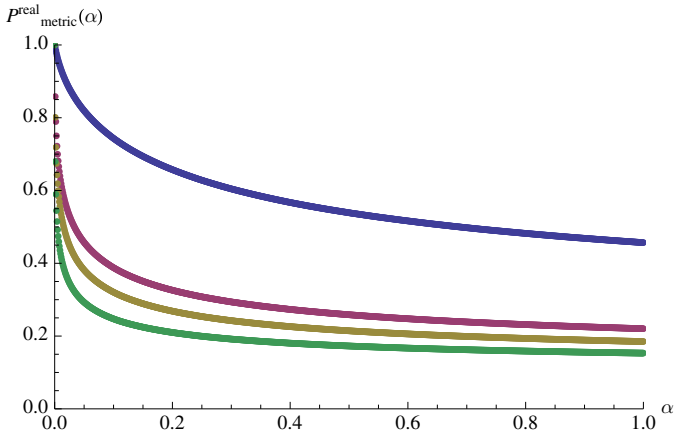

Figure 1. Curves generated by enforcement of determinant-based constraint (4) for the generic 9-dimensional real density matrices. The order of dominance of the four metric-specific curves is given in (5). 17 100 000 Tezuka–Faure 9-dimensional points were employed in the quasi-Monte Carlo numerical integration. The values at $\alpha = 1$ are the embedded (conventional) separability probabilities.

This, of course, will imply that the associated two-qubit *separability* probabilities (corresponding to $\alpha = 1$) adhere to the same ordering. Since the Bures metric is also the *minimal* monotone metric, it is not surprising that it is extremal among the three monotone metrics under consideration. In estimating these curves, as well as all others displayed below involving α—except figure 14—we subdivided the unit interval $\alpha \in [0, 1]$ into 1000 subintervals.

We can fit the Hilbert–Schmidt curve in figure 1 rather well—the integral over $\alpha \in [0, 1]$ of the sum of squares of the differences being only 0.000 265 57—while exactly achieving the conjectured separability probability of $\frac{8}{17}$, with the simple function:

$$P^{\text{real}}_{HS}(\alpha) = \frac{8}{8 + 9\sqrt{\alpha}}. \tag{6}$$

2.1.2. Complex two-qubit density matrices. In figure 2, we analogously show as a function of $\alpha \in [0, 1]$, the four probabilities $\left(P^{\text{complex}}_{\text{metric}}(\alpha)\right)$ for a generic (15-dimensional) complex two-qubit system that the inequality constraint (4) is satisfied. We can fit the Hilbert–Schmidt curve here very well—the integral over $\alpha \in [0, 1]$ of the sum of squares of the differences being only 0.000 300 92—while achieving our conjectured separability probability of $\frac{8}{33}$ [7] with the function

$$P^{\text{complex}}_{HS}(\alpha) = \left(\frac{c}{c + 25\sqrt{\alpha}}\right)^2, \tag{7}$$

where $c = 8 + 2\sqrt{66}$. Also, the *square* of the real counterpart (6) does provide a close fit to the Hilbert–Schmidt curve in figure 2. (However, our conjectured complex two-qubit separability probability of $\frac{8}{33} \approx 0.242\,424$ is not equal to the square, $\frac{64}{289} \approx 0.221\,453$, of the conjectured real separability probability of $\frac{8}{17}$, so conformity to a Dyson-index pattern is not total.)

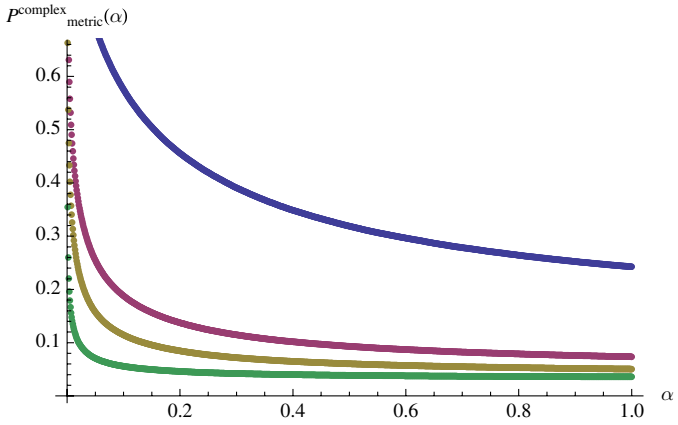

Figure 2. Curves generated by enforcement of determinant-based constraint (4) for the generic 15-dimensional complex density matrices. The order of dominance of the four metric-specific curves is given in (5). 15 400 000 Tezuka–Faure 15-dimensional points were employed in the numerical integration.

Additionally, we can very well fit the Bures curve in figure 2 *and* our corresponding conjectured 'silver mean' separability probability (2) [4] by the function (of the seventh root of α)

$$P^{\text{complex}}_{\text{Bures}}(\alpha) = \frac{1680(1-\sqrt{2})}{\left(4\sqrt{105(-1+\sqrt{2})}(\sqrt[7]{\alpha}-1)+\pi^4\sqrt[7]{\alpha}\right)^2}. \tag{8}$$

(The sum-of-squares measure of fit between the two curves is 0.000 739 208. However, the (exact) square root of (8)—deviating substantially from a Dyson-index-like pattern—does not at all provide a close fit (as in the HS case) to the real *Bures* counterpart in figure 1.)

2.2. *Second set of constraints—convex combinations of minimum eigenvalues of ρ and ρ_{PT}*

2.2.1. Real two-qubit density matrices. In figure 3 we show as a function of $\alpha \in [0, 1]$, the probabilities for a generic (9-dimensional) real two-qubit system that

$$\alpha\lambda_{PT\,\text{min}} + (1-\alpha)\lambda_{\text{min}} \geqslant 0, \tag{9}$$

where the subscript min denotes the smallest of the corresponding four eigenvalues (λ) of either ρ or ρ_{PT}. (As noted, having all eigenvalues nonnegative is fully equivalent to having a nonnegative determinant for the partial transpose of a 4×4 density matrix [34]. The entanglement measure *negativity* is equal to $\max[0, -2\lambda_{PT_{\text{min}}}]$ [16, p 401]. The Hilbert–Schmidt distance of an entangled state to the set of all partially transposed sets can be expressed as a function of the negative eigenvalues of the partial transpose of the entangled state [35].)

2.2.2. Complex two-qubit density matrices. In figure 4 we show as a function of $\alpha \in [0, 1]$, the probabilities for a generic (15-dimensional) complex two-qubit system that the inequality constraint (9) holds. One can fit the complex HS curve rather closely by the *square* of the corresponding real HS curve, particularly so if one adds a small linearly increasing correction of the form $\frac{\alpha}{30}$ to this square.

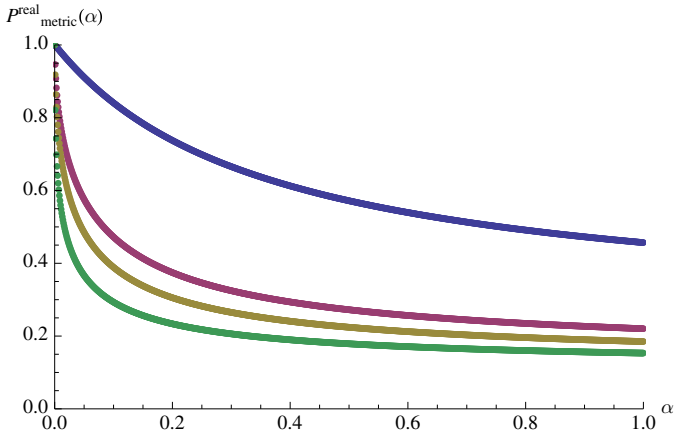

Figure 3. Curves generated by enforcement of minimum-eigenvalue-based constraint (9) for the generic 9-dimensional real density matrices. The order of dominance of curves is given in (5). 32 700 000 Tezuka–Faure 9-dimensional points were employed in the numerical integration.

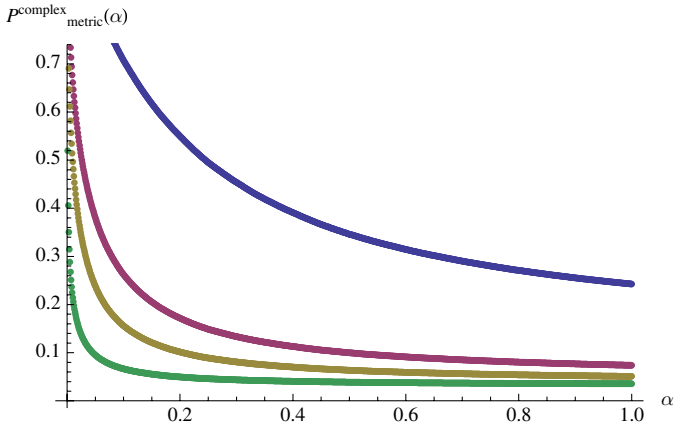

Figure 4. Curves generated by enforcement of minimum-eigenvalue-based constraint (9) for the generic 15-dimensional complex density matrices. The order of dominance of curves is given in (5). 18 450 000 Tezuka–Faure 15-dimensional points were employed.

2.3. Third set of constraints—determinants of convex combinations of ρ and ρ_{PT}

2.3.1. Real two-qubit density matrices. In figure 5 we show as a function of $\alpha \in [0, 1]$, the probabilities for a generic (9-dimensional) real two-qubit system that the positive 'twofold partial' transpose condition,

$$|\alpha\rho_{PT} + (1 - \alpha)\rho| \geqslant 0, \tag{10}$$

holds. The Hilbert–Schmidt curve is highly linear in character. The line $1 - \frac{9\alpha}{17}$ closely approximates it, as well as reproducing the conjectured separability probability of $\frac{8}{17}$.

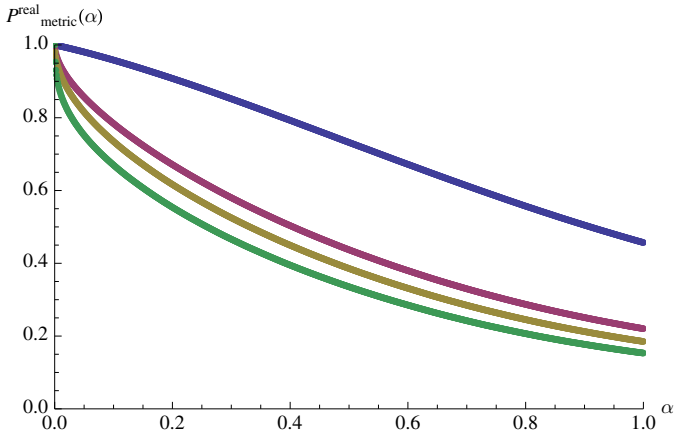

Figure 5. Curves generated by enforcement of determinant constraint (10) for the generic 9-dimensional real density matrices. The order of dominance of curves is given in (5). 22 500 000 TF 9-dimensional points were employed.

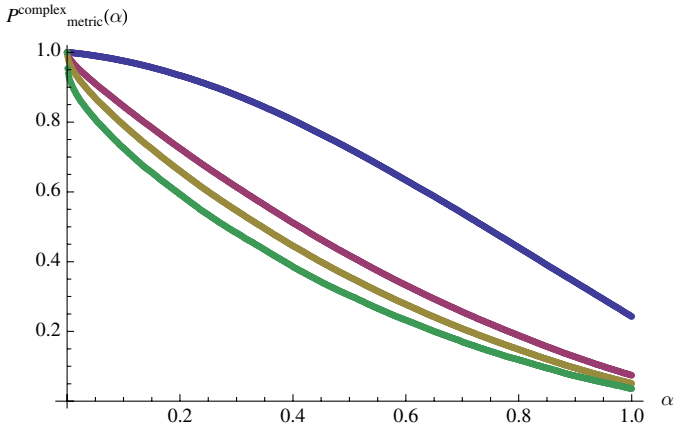

Figure 6. Curves generated by enforcement of determinant constraint (10) for the generic 15-dimensional complex density matrices. The order of dominance of curves is given in (5). 14 520 000 TF 15-dimensional points were employed.

2.3.2. Complex two-qubit density matrices. In figure 6 we show as a function of $\alpha \in [0, 1]$, the four probabilities $\left(P^{\text{complex}}_{\text{metric}}(\alpha)\right)$ for a generic complex two-qubit system that the inequality (9) holds.

In computing figures 5 and 6, we solve the quartic equation $|\alpha\rho_{PT} + (1 - \alpha)\rho| = 0$ and assume that there cannot be more than one solution $\alpha \in [0, 1]$. (Numerically, this did appear to be the case, except for some isolated instances in which two positive (essentially identical) roots both very close to zero were found.)

Another possible generalized Peres–Horodecki condition—that is, that the minimum eigenvalue of $\alpha\rho_{PT} + (1 - \alpha)\rho$ be nonnegative—appeared to be considerably more problematical (time-consuming) than (10) to investigate, though we do, in fact, implement such a condition for the generic complex qubit–qutrit systems (section 4) and in generating figure 14.

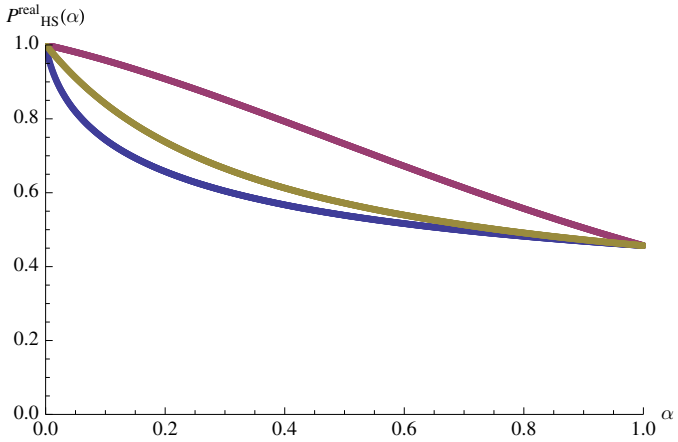

Figure 7. The curves corresponding to the Hilbert–Schmidt metric plotted above for the three *different* constraints for the generic real 9-dimensional two-qubit systems. The quasi-linear curve based on constraint (10) dominates that based on (9), which dominates that based on (4).

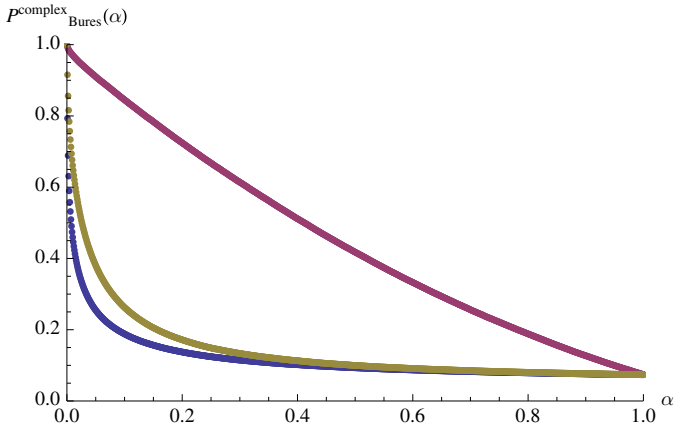

Figure 8. The curves corresponding to the Bures metric plotted above for the three *different* constraints for the generic complex 15-dimensional two-qubit systems. The curve based on constraint (10) dominates that based on (9), which dominates that based on (4).

Let us note that all the curves displayed so far in this communication appear to correspond to *convex* functions, but for the last two Hilbert–Schmidt curves.

2.4. Comparison of metric-specific curves for the first three sets of constraints

In figure 7 we show in a single plot, the three Hilbert–Schmidt curves plotted above (one per figure) for the generic real 9-dimensional two-qubit systems, while in figure 8 we show in a single plot, the three Bures curves plotted above for the generic complex 15-dimensional two-qubit systems. In both these figures the order of dominance of the curves is the same—the curve based on the constraint (10) dominates that based on (9), which, in turn, dominates that based on (4).

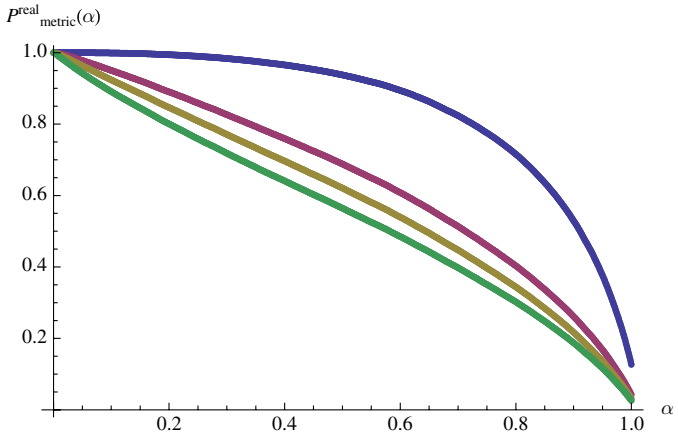

Figure 9. Curves generated by enforcement of *modified* (3×3 principal minor) constraint (4) for the generic 14-dimensional rank-3 complex density matrices. The order of dominance of curves is given in (5). 7 300 000 TF 14-dimensional points were employed.

Of course, we find in both of these figures that the three curves have common points-of-intersection at $\alpha = 1$, corresponding to the 'ordinary' separability probability (as well as $\alpha = 0$).

3. Generic rank-3 complex two-qubit case

The 'twofold' volume-to-area-ratio theorem of Szarek, Bengtsson and Życzkowski [36] allows us to immediately extend our conjecture [7] of Hilbert–Schmidt separability probability of $\frac{8}{33}$ for the 15-dimensional generic complex two-qubit states to the fully equivalent conjecture that the HS separability probability of the states on the 14-dimensional boundary is *one-half* of this, that is, $\frac{4}{33}$. In figures 9 and 10, we show our corresponding estimation of the α-separabilities based on certain obvious modifications of the determinant constraint (4) and the minimum eigenvalue constraint (9). That is, rather than using the (zero) determinant of the rank-3 density matrix, we use its generically nonzero 3×3 principal minor. Further, rather than using the minimum (zero) eigenvalue, we employ the minimum of the generically three nonnegative eigenvalues.

In figure 11, we display the rank-3 α-separability probability estimates based on the application of the constraint (10). Here we notice some unusual behavior near $\alpha = 0$ due to the degeneracy (zero determinant) of a rank-3 two-qubit (4×4) density matrix.

4. Generic full-rank complex qubit–qutrit case

Of the three distinct sets of constraints considered in the two-qubit case, only (9) seemed immediately adoptable to the qubit–qutrit case associated with 6×6 density matrices. In our computations, we now employ the associated $SU(6)$ Euler-angle parameterization [21, section 11]. In figure 12 we show the corresponding plot.

Further, by specifically checking nonnegativity at each value of $\alpha = \frac{1}{1000}, \ldots 1$, we were able to enforce the condition that the minimum eigenvalue of the matrix convex combination $\alpha\rho_{PT} + (1-\alpha)\rho$ be nonnegative. (Nonnegativity of the determinant of the partial transpose is no

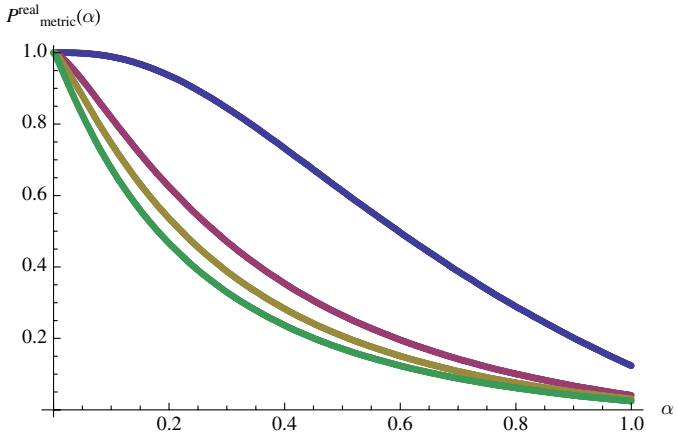

Figure 10. Curves generated by enforcement of *modified* (minimum-eigenvalue-based) constraint (9) for the generic 14-dimensional rank-3 complex density matrices. The order of dominance of curves is given in (5). 10 300 000 TF 14-dimensional points were employed.

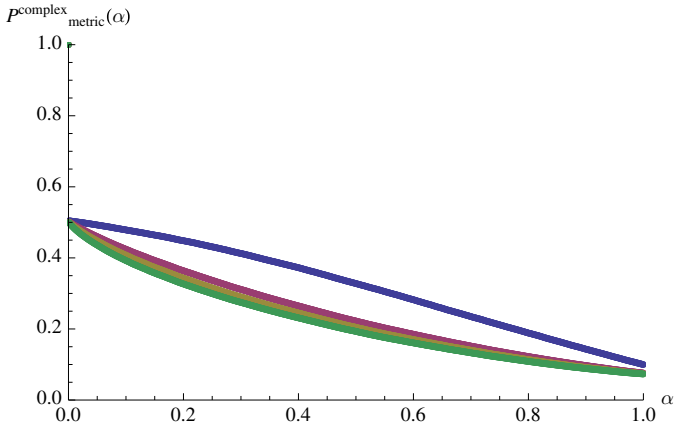

Figure 11. Curves generated by enforcement of constraint (10) for the generic 14-dimensional rank-3 complex density matrices. The order of dominance of curves is given in (5). 4 300 000 TF 14-dimensional points were employed.

longer equivalent—as it is in the two-qubit case [34]—to having no negative eigenvalues, since *two* negative eigenvalues yield a *positive* determinant.) The corresponding plot is displayed in figure 13.

We can 'sandwich' the Hilbert–Schmidt curve in figure 12 between two curves, corresponding to exact squares, both of which yield the conjectured separability probability of $\frac{32}{1199}$. These functions are

$$\frac{64}{((-8+\sqrt{2398})\sqrt{\alpha}+8)^2} \quad \text{and} \quad \frac{64}{((-8+\sqrt{2398})\alpha+8)^2}. \tag{11}$$

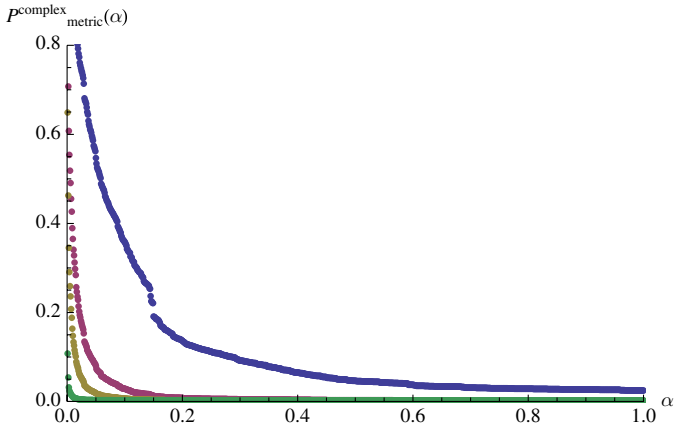

Figure 12. Curves generated by enforcement of (minimum-eigenvalue-based) constraint (9) for the generic 35-dimensional complex 6×6 density matrices. The order of dominance of curves is given in (5). 30 650 000 TF 35-dimensional points were employed.

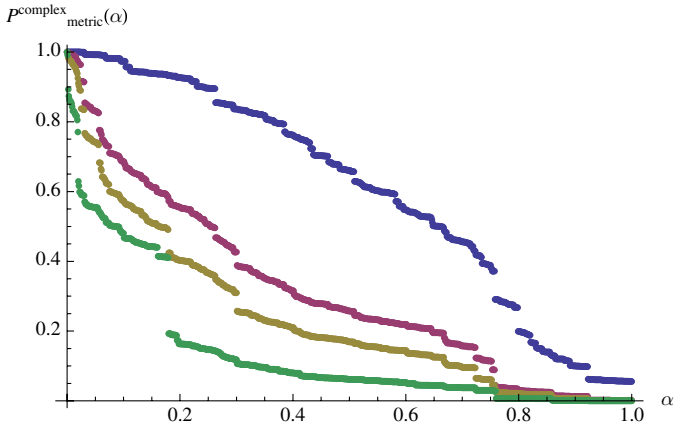

Figure 13. Curves generated by verifying the nonnegativity of the minimum eigenvalue of $\alpha\rho_{PT} + (1-\alpha)\rho$ for the generic complex qubit–qutrit systems. The order of dominance of curves is given in (5). 1 300 000 TF 35-dimensional points were employed.

5. Extending range of α-parameter

We have, so far, considered our primary variable α as extending over the unit interval $[0, 1]$. However, it appears quite interesting and possibly more natural to formally view its range as the real line $[-\infty, \infty]$. In a further analysis, we developed a plot (figure 14) over $\alpha \in \left[-\frac{9}{4}, \frac{11}{4}\right]$, of the estimated α-probability that the 4×4 matrix $\alpha\rho_{PT} + (1-\alpha)\rho$, where ρ is a generic complex two-qubit density matrix, has all its four eigenvalues nonnegative.

6. Concurrence-related analyses

6.1. Generalized Peres–Horodecki conditions

In all the analyses reported above, the nonnegativity convex combination constraints ('generalized Peres–Horodecki conditions') utilized have been expressed either in terms of the

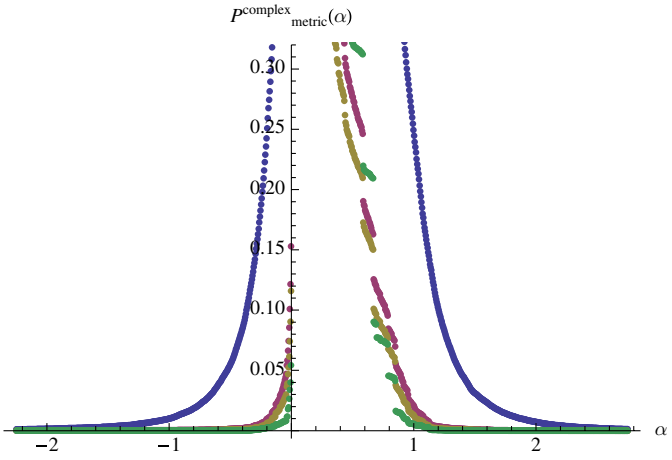

Figure 14. Curves generated by verifying the nonnegativity of the minimum eigenvalue of $\alpha\rho_{PT} + (1-\alpha)\rho$ for the generic complex two-qubit systems, using the *extended* interval $\alpha \in [-\frac{9}{4}, \frac{11}{4}]$. The order of dominance of curves is given in (5). 1 650 000 TF 15-dimensional points were employed.

determinant or the minimum eigenvalue of ρ_{PT}. In the two-qubit case, we have also been able to investigate similarly motivated conditions using, in conjunction, the *maximal concurrence* over spectral orbits (1) [24] of a two-qubit density matrix (ρ), and its *concurrence* [22]

$$C = \max(0, \eta_1 - \eta_2 - \eta_3 - \eta_4), \qquad (\eta_1 \geqslant \eta_2 \geqslant \eta_3 \geqslant \eta_4). \tag{12}$$

(Here, the λ's are the ordered eigenvalues of ρ and the η's are the ordered eigenvalues of $\sqrt{\sqrt{\rho}\tilde{\rho}\sqrt{\rho}}$, where $\tilde{\rho} = (\sigma_y \otimes \sigma_y)\rho^*(\sigma_y \otimes \sigma_y)$, and $\sigma_y \equiv \sigma_2$ is a Pauli matrix, and $*$ denotes conjugation. Throughout the reminder of the paper, the symbol σ—consistently with our previous notation—will denote a 'separability function', and not a Pauli matrix.) The corresponding constraint we employ is

$$-\alpha C + (1-\alpha)C_{\max} \geqslant 0. \tag{13}$$

Since $C_{\max} \geqslant C$, the constraint holds trivially for $\alpha \in \left[0, \frac{1}{2}\right]$. In figures 15 and 16, we show for the *half*-interval $\alpha \in \left[\frac{1}{2}, 1\right]$, the curves for the generic real and complex two-qubit states, respectively, based on (13), while in figures 17 and 18, we display the corresponding plots for the generic rank-3 real and complex two-qubit states, respectively.

6.2. Separability probabilities as functions of concurrence—intersecting curves

In this section, we depart from the basic paradigm so far employed in the first basic part ('generalized Peres–Horodecki conditions') of the paper, in which we use convex combinations of quantum-mechanical terms to form nonnegativity constraints.

Now, we simply estimate—again, with respect to the four metrics in question—the separability probability of two-qubit states for which the concurrence C is less than some threshold C_0. We show our results in figures 19 and 20. The generic rank-3 counterparts of these two figures are given in figures 21 and 22. In all four of these cases, the Hilbert–Schmidt curve intersects the curves for the three monotone metrics from below. In this regard, it has

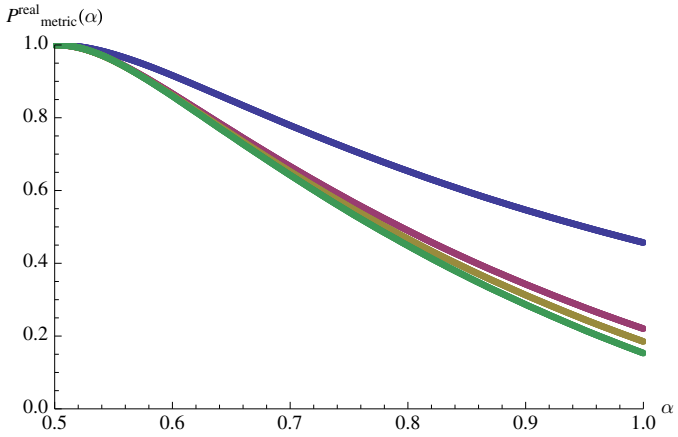

Figure 15. Implementation of concurrence-based constraint (13) for the generic 9-dimensional real two-qubit states. The order of dominance of curves is given in (5). 9 250 000 TF-points were employed.

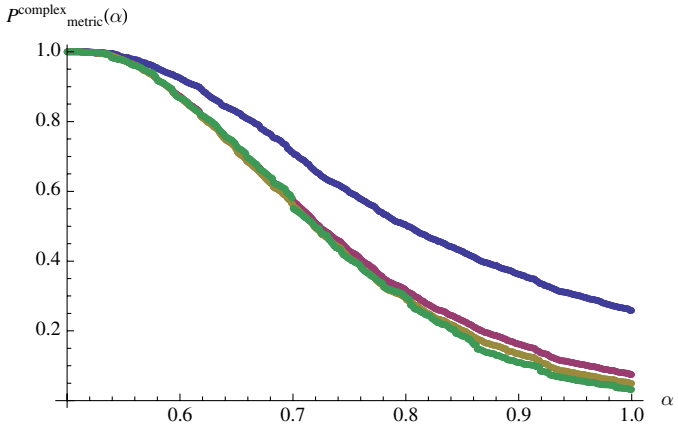

Figure 16. Implementation of concurrence-based constraint (13) for the generic 15-dimensional complex two-qubit states. The order of dominance of curves is given in (5). 6 100 000 TF-points were employed.

been noted by Bengtsson and Życzkowski that the 'Bures measure is concentrated at the states of higher (than the Hilbert–Schmidt) purity' [16, p 356], since $\langle \text{Tr}\rho^2 \rangle_{HS} < \langle \text{Tr}\rho^2 \rangle_{\text{Bures}}$. Our (intersecting) results in this set of concurrence-based analyses are clearly consistent—but now taking a separability-related form—with that assertion.

7. Remarks

Our motivation in undertaking the first principal part of this study reported above has been to examine whether it might be feasible to shift the question of determining the two-qubit separability probabilities with respect to various metrics of quantum-mechanical interest to the (perhaps more tangible, addressable) question of characterizing the *curves* that *interpolate* between such separability probabilities and the (unit) probabilities that a two-qubit state is

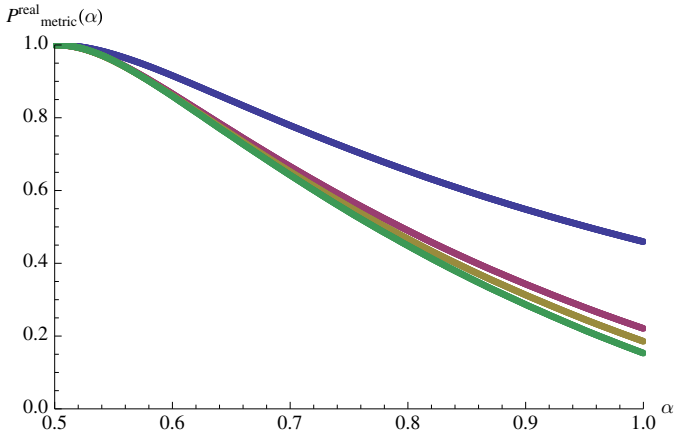

Figure 17. Implementation of concurrence-based constraint (13) for the generic 8-dimensional real rank-3 two-qubit states. 10 300 000 TF-points were employed.

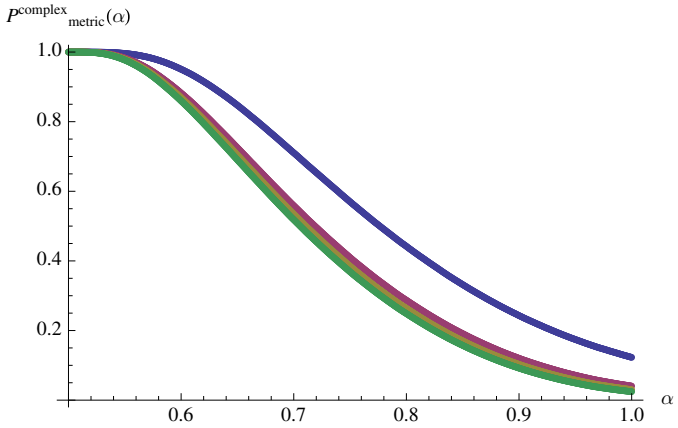

Figure 18. Implementation of concurrence-based constraint (13) for the generic 14-dimensional complex rank-3 two-qubit states. 11 950 000 TF-points were employed.

either separable *or* entangled (cf [13, 14]). We intend to study the curves generated in still greater detail, as additional computations render them more precise. (The Tezuka–Faure procedure is not amenable to the use of *statistical* tests, though variants of this quasi-Monte Carlo method have been developed that are.) In particular, it would be of interest to see if the differences between the curves for the three monotone metrics studied could be explained directly in terms of the Chentsov–Morozova functions $c(x, y)$ for those metrics [26, 37]. These are $\frac{2}{x+y}$, $\frac{4}{(\sqrt{x}+\sqrt{y})^2}$ and $\frac{(\log x - \log y)}{x-y}$, for the Bures, Wigner–Yanase and Kubo–Mori metrics, respectively. (The associated operator monotone functions, $f(t)$, for which $c(x, y) = \frac{1}{y f(\frac{x}{y})}$ are $\frac{1+t}{2}$, $\frac{t+2\sqrt{t}+1}{4}$ and $\frac{t-1}{\log t}$, respectively.) The possible relevance of the Dyson-index-*ansatz* to explain differences between results for the generic real and generic complex systems—as given in section 8 below—should also be examined [7, 17].

Conceiveably, our attempted generalizations here of the Peres–Horodecki conditions and introduction of the concept of 'α-separability' might prove productive in some manner

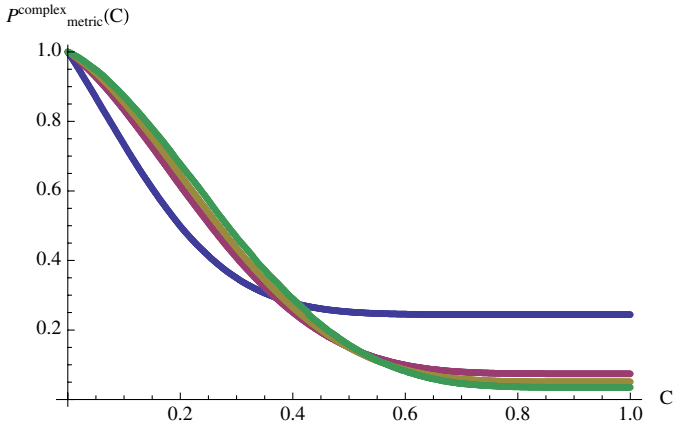

Figure 19. Separability probabilities of generic complex two-qubit states having concurrence less than or equal to C. The Hilbert-Schmidt (blue) curve intersects the other three. 21 100 000 TF-points were employed.

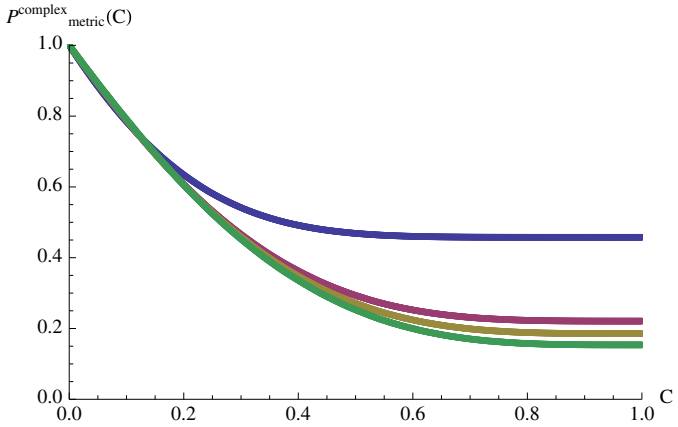

Figure 20. Separability probabilities of generic real two-qubit states having concurrence less than or equal to C. The Hilbert-Schmidt (blue) curve intersects the other three from below, all near $\alpha = 0.12$. There were 7 800 000 TF-points employed.

parallel to the well-studied concepts (also based on generalizations/extensions/embeddings) of p-Rényi-entropy [38] and of escort distributions [39, 40].

8. Separabilities as piecewise continuous functions of maximal concurrence

8.1. Objective

Here, we begin the second basic part of our paper. We importantly amend a certain parenthetical remark made in our recent paper [17] to the effect that although two-qubit *diagonal-entry*-parameterized separability functions (DESFs) had been shown [7, 31] to clearly conform to a pattern dictated by the 'Dyson indices' ($\beta = 1$ (real), 2 (complex), 4 (quaternionic)) of random matrix theory, this did not appear to be the case with regard to *eigenvalue*-parameterized

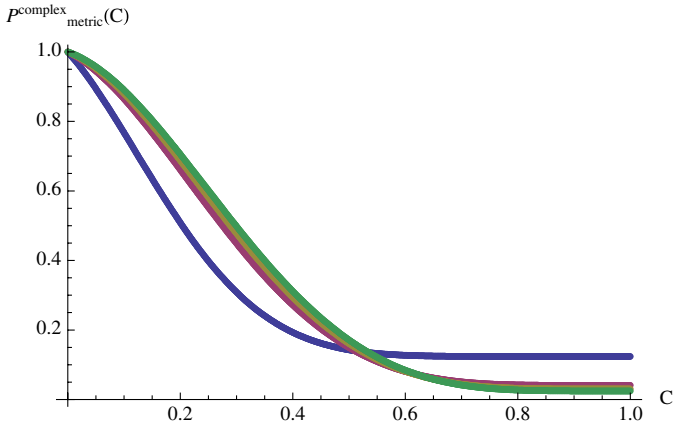

Figure 21. Separability probabilities of generic rank-3 complex two-qubit states having concurrence less than or equal to C. The Hilbert–Schmidt (blue) curve intersects the other three. 14 000 000 TF-points were employed.

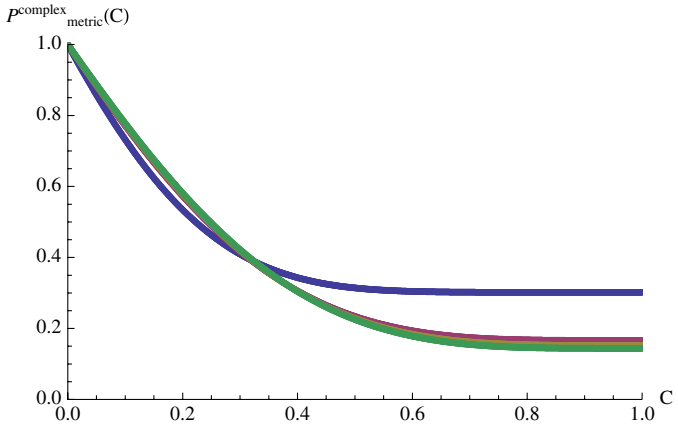

Figure 22. Separability probabilities of generic rank-3 real two-qubit states having concurrence less than or equal to C. The Hilbert–Schmidt (blue) curve intersects the other three. 9 750 000 TF-points were employed.

separability functions (ESFs). (We remark here that the 'value of β is given by the number of independent degrees of freedom per matrix element and is determined by the antiunitary symmetries . . . It is a concept that originated in Random Matrix Theory and is important for the Cartan classification of symmetric spaces' [41, p 480]. The Dyson index corresponds to the 'multiplicity of ordinary roots', in the terminology of symmetric spaces [42, table 2].) But upon further examination of the extensive numerical analyses reported in [17], we found quite convincing evidence that adherence to the Dyson-index pattern does also hold for ESFs, at least as regards the upper *half*-range $\frac{1}{2} \leqslant C_{\max} \leqslant 1$ of the maximal concurrence over spectral orbits (1).

To be specific, it strongly appears that in this upper half-range, the *real* two-qubit ESF is equal to $\frac{(2-2C_{\max})^{\frac{3}{2}}}{\sqrt{30}}$, and its *complex* counterpart—in conformity to the Dyson-index pattern—proportional to the *square* of the real ESF, that is, $\frac{(2-2C_{\max})^3}{15}$. The previously documented

piecewise continuous ('semilinear') behavior in the *lower* half-range $0 \leqslant C_{\max} \leqslant \frac{1}{2}$ appeared to lack any particular Dyson-index-related interpretation—which seemed somewhat paradoxical in terms of our DESF-findings [7, 31]. However, we report new insights into this problem below (section 9.3).

8.2. Previous ESF findings

The study [17] had been devoted to the question of determining for the generic (9-dimensional) real and (15-dimensional) complex two-qubit systems, the nature of certain trivariate 'eigenvalue-parameterized separability functions' (ESFs). These (metric-*independent*) ESFs, it was argued, could substantially assist in the determination of separability *probabilities* in terms of certain metrics (the Hilbert–Schmidt and Bures being the most conspicuous examples). (In [7], DESFs were successfully used in the Hilbert–Schmidt case, but they do not seem as useful for the Bures and other montone metrics, the standard formulas for which are expressed in terms of eigenvalues, and *not* diagonal entries.) We further investigated in [17] the possibility that these *prima facie* trivariate functions of the eigenvalues λ_i $(i = 1, \ldots, 4)$ of 4×4 density matrices $\left(\lambda_4 = 1 - \Sigma_i^3 \lambda_i\right)$ were expressible as *univariate* functions:

$$S_4^{(\beta)}(\lambda_1 \ldots \lambda_4) = \sigma^{(\beta)}(C_{\max}(\lambda_1 \ldots \lambda_4)), \tag{14}$$

of the *maximal concurrence* $C_{\max}$—given by (1)—over spectral orbits [24, section 7] [43, 44]. (At this point in our presentation, let us—motivated by Dyson-index conventions—regard β in (14) only as a notational (dummy variable), not calculational device taking the values 1 (real), 2 (complex), 4 (quaternionic).)

8.3. Jump discontinuities

Our main conclusions in [17] were that—if the reducibility-to-univariance property (14) held, as our extensive numerical evidence appeared to suggest might be the case (being able to explain almost 99% of the variance [17, section II.B.1])—the associated real and complex univariate functions both had jumps of approximately 50% magnitude at $C_{\max} = \frac{1}{2}$, as well as a number of additional discontinuities (remarkably coincident in both the real and complex cases) in the *lower* half-range $C_{\max} \in \left(0, \frac{1}{2}\right]$. (The joint jumps at $C_{\max} = \frac{1}{2}$ were displayed in [17] in figures 2 and 6. We have since found a small programming error that caused the two curves in figure 2 there to be slightly more misaligned—by $\frac{1}{500}$—than they should have been.) Also, both univariate functions appeared to be simply *linear* between certain of these discontinuities. The *upper* half-range $C_{\max} \in \left[\frac{1}{2}, 1\right]$—in which the univariate functions of $C_{\max}$ took lesser values—did not command our attention in [17], seeming to be of relatively less interest. Our only pertinent observation there was that there did not appear to be any discontinuities in that segment.

8.4. New Dyson-index-related findings

Now, in fact, turning our attention more closely to this upper half-range $C_{\max} \in \left[\frac{1}{2}, 1\right]$, we readily find strong evidence for a very interesting Dyson-index-type phenomenon. If we *normalize* our extensive numerical estimates from [17] of $\sigma^1(C_{\max})$ and $\sigma^2(C_{\max})$ to both equal to 1 at the *jump* discontinuity point $C_{\max} = \frac{1}{2}$, then a joint plot (figure 23) of the latter normalized (complex) function versus the *square* of the former normalized (real) function for $C_{\max} \in \left[\frac{1}{2}, 1\right]$ remarkably shows *no* perceptible difference between the two resulting curves. (The sample (quasi-Monte Carlo) estimate of $\sigma^2\left(\frac{1}{2}\right)$ is 0.065 1586 and that of $\sigma^1\left(\frac{1}{2}\right)$) is

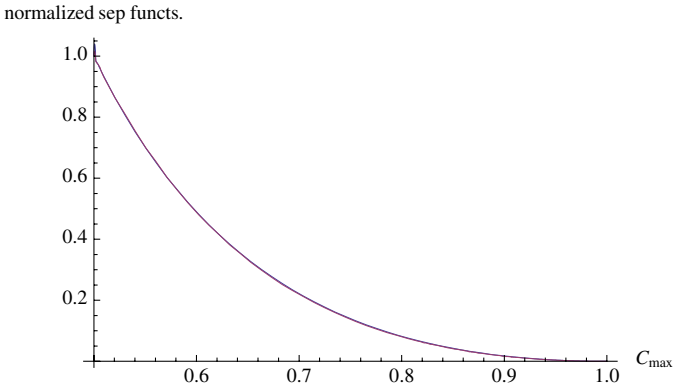

Figure 23. *Joint* plot of numerical estimates of $(\frac{\sigma^1(C_{\max})}{\sigma^1(\frac{1}{2})})^2$ *and* $\frac{\sigma^2(C_{\max})}{\sigma^2(\frac{1}{2})}$ for $C_{\max} \in [\frac{1}{2}, 1]$.

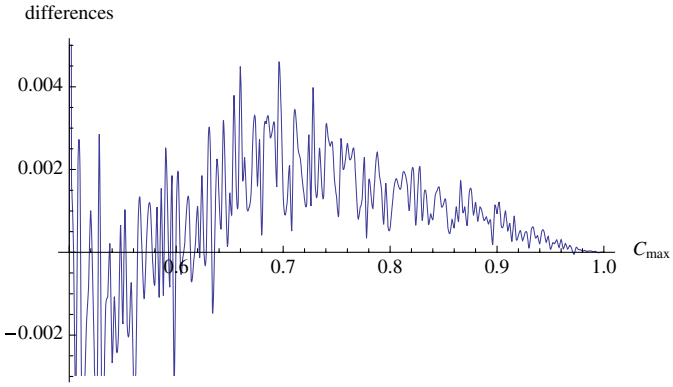

Figure 24. Numerical estimate of $(\frac{\sigma^1(C_{\max})}{\sigma^1(\frac{1}{2})})^2 - \frac{\sigma^2(C_{\max})}{\sigma^2(\frac{1}{2})}$.

0.180 3748.) In figure 24, we show—on a much finer scale than used in figure 23—the actual (very small) numerically obtained differences:

$$\left(\frac{\sigma^1(C_{\max})}{\sigma^1\left(\frac{1}{2}\right)}\right)^2 - \frac{\sigma^2(C_{\max})}{\sigma^2\left(\frac{1}{2}\right)}, \tag{15}$$

between them. Of further considerable importance, figure 25 is a repetition of figure 23, but along with the insertion now of the function

$$(2 - 2C_{\max})^3 = 8(1 - C_{\max})^3, \tag{16}$$

which we see fits our two estimates *very* well. Assuming that (16) is the correct form (up to the still not exactly known normalization factor) of $\sigma^2(C_{\max})$ over $C_{\max} \in \left[\frac{1}{2}, 1\right]$, we can estimate the associated contribution to the separability probabilities from density matrices corresponding to this half-range to the Hilbert–Schmidt and Bures separability probabilities of generic complex two-qubit systems to be 0.010 0578 and 0.019 4829, respectively. (The real counterparts of these separability probabilities are, then, 0.025 4346 and 0.010 0578, respectively (cf (29), (30)).)

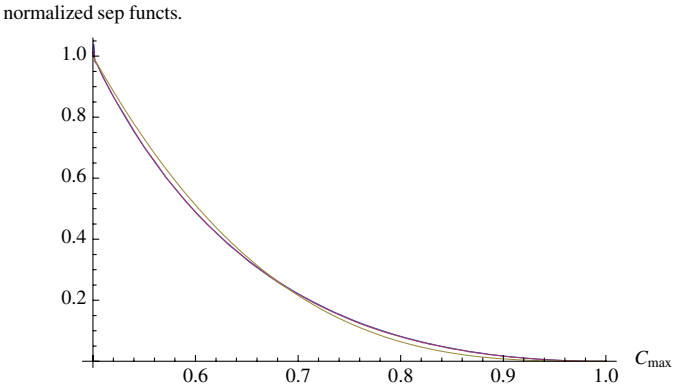

Figure 25. The two functions in figure 23, along with the additional (*very* closely-fitting) function $(2 - 2C_{\max})^3$.

Let us further note that our sample estimate of the ratio

$$\frac{\sigma^2\left(\frac{1}{2}\right)}{\left(\sigma^1\left(\frac{1}{2}\right)\right)^2} = \frac{0.065\,1586}{0.180\,3748^2} = 2.002\,72 \tag{17}$$

is very close (and possibly theoretically exactly equal) to 2.

Over $0 \leqslant C_{\max} \leqslant \frac{1}{2}$, the range of primary interest in [17], the estimates of the real and complex two-qubit separability functions *intersect* (near $C_{\max} = 0.1812$), and appear to have linear segments over the *same* subintervals [17, figures 1, 5, 7]. These features appeared to make any immediate application of the Dyson-index pattern problematical in this lower half-range. So, the behaviors of the univariate functions $\sigma^{(\beta)}(C_{\max})$ ($\beta = 1$ (real), 2 (complex)) over the two indicated regimes of $C_{\max}$ seem to be highly distinct. The point $C_{\max} = \frac{1}{2}$ clearly serves as a point of major behavioral transition, with the lower half-range, then, appearing perhaps to be the more theoretically challenging of the two. (We will observe what appears to be similarly dichotomous Dyson-index behavior in the qubit–qutrit case (figure 31). Perhaps one might view the two regimes as semiclassical and quantum in nature.)

An outstanding question is what are the specific values of $\sigma^1\left(\frac{1}{2}\right)$ and $\sigma^2\left(\frac{1}{2}\right)$, which we used as normalization factors in our analyses above. The nearness to 2 of the ratio (17) may be a helpful guide in this regard. In fact, let us take this opportunity to further indicate that in our ongoing supplemental analyses—in which we use 5000, rather than 500 sampling points in the interval [0, 1]—we have obtained for the ratio (17) the estimate

$$\frac{\sigma^2\left(\frac{1}{2}\right)}{\left(\sigma^1\left(\frac{1}{2}\right)\right)^2} = \frac{0.066\,663}{0.182\,75^2} = 1.996\,05. \tag{18}$$

This ratio would be exactly 2 if we took for the numerator of (18) the value $\frac{1}{15} \approx 0.066\,6667$ and for the denominator, $\frac{1}{30} \approx 0.182\,574^2$. We will, in fact, assume these exact values in seeking to ascertain in section 9, the exact contributions over $C_{\max} \in \left[\frac{1}{2}, 1\right]$ to the total Hilbert–Schmidt two-qubit generic real and complex separability probabilities.

8.5. Rank-3 complex and real two-qubit cases

Here, we apply the same maximal-concurrence ansatz (14) just discussed and applied to the full (rank-4) complex and real two-qubit cases, to the minimally degenerate (rank-3) counterparts. The main conceptual point to note is that the formula for the maximal concurrence (1) now

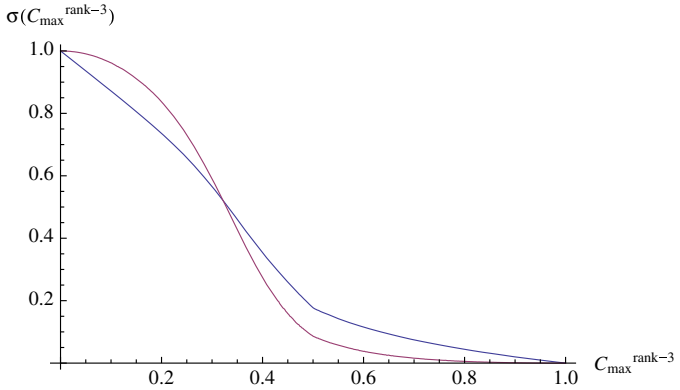

Figure 26. Eigenvalue-parameterized separability functions, expressed in terms of maximal concurrence, for the *minimally degenerate rank-3* generic real and complex two-qubit states. The complex (red) curve is initially dominant. For each TF-point employed (2 062 400 in the complex case and 2 331 300 in the real case), separability is checked for 500 equally spaced values of $C_{\max}^{\text{rank-3}}$. There appear to be discontinuities at $C_{\max}^{\text{rank-3}} = \frac{1}{2}$.

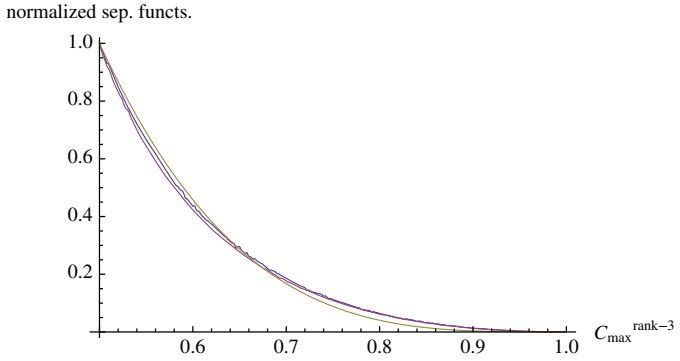

Figure 27. The rank-3 counterpart to figure 25, with the rather well-fitting function $(2-2C_{\max}^{\text{rank-3}})^{\frac{7}{2}}$ replacing $(2-2C_{\max}^{\text{rank-4}})^3$.

degenerates to

$$C_{\max}^{\text{rank-3}} = \lambda_1 - \lambda_3, \qquad (\lambda_1 \geqslant \lambda_2 \geqslant \lambda_3). \tag{19}$$

In figure 26 we show the joint plot of the corresponding real and complex curves. The estimated complex (red) curve initially dominates the estimated real (blue) curve (cf [17, figure 1]).

8.5.1. Close resemblance to generic rank-4 Dyson-index pattern. It appears now—as a plot (figure 27) parallel to that displayed in figure 25—that the Dyson-index pattern continues to hold for the range $C_{\max}^{\text{rank-3}} \in \left[\frac{1}{2}, 1\right]$ in the two-qubit generic rank-3 cases, but with the replacement of $\left(2-2C_{\max}^{\text{rank-4}}\right)^3$ by $\left(2-2C_{\max}^{\text{rank-3}}\right)^{\frac{7}{2}}$.

To test the possible applicability of the rank-3 version of the univariance hypothesis (14), we estimated the real and complex rank-3 two-qubit Hilbert–Schmidt separability probabilities using the ESFs displayed in figure 26. The values we obtained were 0.208 172 and 0.104 852, respectively (while the corresponding conjectured values were perhaps somewhat

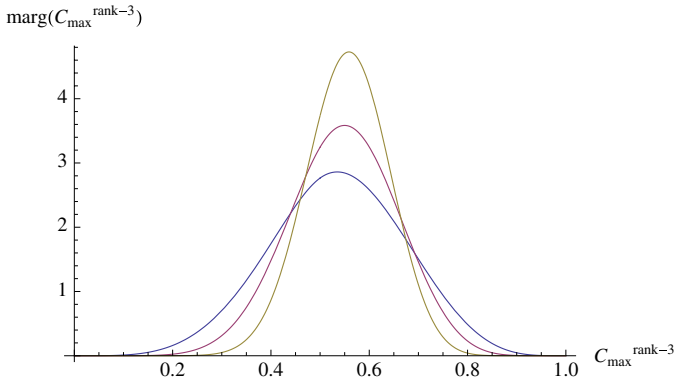

Figure 28. Univariate marginal probability distributions (20) and (21) over $C_{\max}^{\text{rank-3}}$ of the Hilbert–Schmidt measures on the eigenvalues. The quaternionic curve has the highest peak and the real curve, the lowest. All three curves are asymmetric about $C_{\max}^{\text{rank-3}} = \frac{1}{2}$ and skewed to the right. The real peak (mode) is at 0.534 989, the complex at 0.549 857, and the quaternionic at 0.558 738, while the medians are 0.537 07, 0.5483 and 0.556 787, respectively. Also, the means are $\frac{781}{2\cdot 3^6} \approx 0.535\,665$, $\frac{35}{2^6} \approx 0.546\,875$ and $\frac{27\,313}{2^{14}\cdot 3} \approx 0.555\,684$, respectively.

disappointingly different, calling for further analysis, that is $\frac{4}{17} \approx 0.235\,294$ and $\frac{4}{33} \approx 0.121\,212$). We can express these results as *one*-dimensional integrals over $C_{\max}^{\text{rank-3}} \in [0, 1]$ of the product of the real function displayed in figure 26, and (using $C \equiv C_{\max}^{\text{rank-3}}$) the univariate marginal Hilbert–Schmidt probability distribution (figure 28):

$$\text{marg}_{\text{real}}(C) = \begin{cases} -\frac{1792}{81} C^4 (12C^2 - 5) & 0 < C \leqslant \frac{1}{2} \\ \frac{3584}{81} (C-1)^4 C (4C(5C-1) - 1) & \frac{1}{2} < C < 1 \end{cases} \tag{20}$$

and the integral over $C_{\max}^{\text{rank-3}} \in [0, 1]$ of the product of the complex function displayed in figure 26, and the univariate marginal Hilbert–Schmidt probability distribution (figure 28):

$$\text{marg}_{\text{complex}}(C) = \begin{cases} -\frac{7280}{729} (C-1)^7 C^2 (C(C(C(16\,325C - 7693) - 379) + 315) + 45) & \frac{1}{2} < C < 1 \\ \frac{7280}{729} C^7 \left(155C^6 + 1287C^4 - 1089C^2 + 231\right) & 0 < C \leqslant \frac{1}{2}. \end{cases} \tag{21}$$

(These distributions are 'marginal', in the sense that they are obtained by integrating the HS or Bures measure defined on the 3-dimensional simplex of eigenvalues—obtainable from the papers of Życzkowski and Sommers [13, 14]—over two of the three coordinates (the third coordinate being $C_{\max}$) used to parameterize the simplex.) Also, we have for $0 < C < \frac{1}{2}$,

$$\text{marg}_{\text{quaternionic}}(C) = \frac{920\,9200 C^{13} (3(7133C^{10} + 236\,790C^8 + 253\,023C^6 - 729\,980C^4 + 497\,097C^2 - 142\,766)C^2 + 46\,189)}{531\,441}. \tag{22}$$

(The quaternionic expression for $\frac{1}{2} < C < 1$ is somewhat more cumbersome in nature to present.) To obtain these univariate functions, we have transformed one of the eigenvalues, say λ_1 to $C_{\max}^{\text{rank-3}} \equiv \lambda_1 - \lambda_3$ (the jacobian of the transformation being unity) and integrated (restricted to the Weyl chamber of ordered eigenvalues) the corresponding (bivariate in this case) Hilbert–Schmidt measures (over the eigenvalues) [13, equations (4.1), (6.5), (7.8)] over λ_2. Fitting the means and variances of ((20)–(22)), we can obtain beta distribution $B(p,q)$ approximations to the real, complex and quaternionic probability distributions using the paired sets of parameters $\{p, q\} = \left\{\frac{47\,641}{7196}, \frac{41\,297}{7196}\right\} \approx$

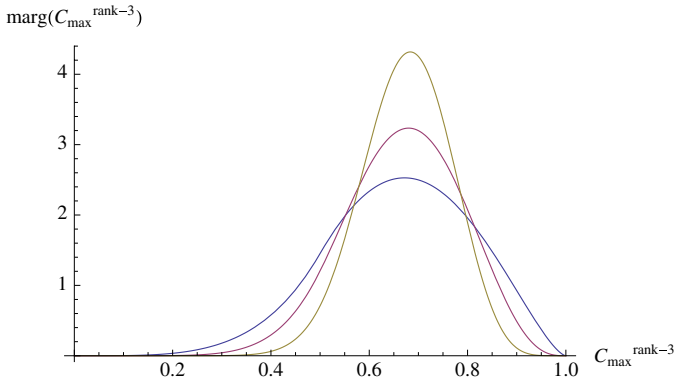

Figure 29. Counterpart to figure 28 based on the Bures metric. The order of curves is the same. Numerical methods were employed.

$\{6.620\,48, 5.738\,88\}$, $\left\{\frac{12\,323\,885}{114\,2816}, \frac{10\,211\,219}{114\,2816}\right\} \approx \{10.7838, 8.935\,14\}$ and $\left\{\frac{4108\,424\,031\,600\,889}{214\,515\,575\,216\,232}, \frac{3285\,024\,436\,207\,367}{214\,515\,575\,216\,232}\right\} \approx \{19.1521, 15.3137\}$, respectively. Beta distributions, defined over the unit interval, are a general type of statistical distribution, related to the gamma distribution, and have two free parameters.

The Hilbert–Schmidt (total–separable and nonseparable) probability that a minimally degenerate two-qubit state has maximal concurrence within the range $\left[\frac{1}{2}, 1\right]$ is $\frac{49}{81} = \left(\frac{7}{9}\right)^2 \approx 0.604\,938$ for real states, $\frac{996\,431}{2^{11}\cdot 3^6} \approx 0.667\,405$ for complex states, and $\frac{3335\,170\,241\,153}{2^{23}\cdot 3^{12}} \approx 0.748\,123$ for quaternionic states. (For the (smaller) full-rank counterparts see section 9.4.) In figure 29, we show the counterpart to figure 28 based on the Bures (minimal monotone) metric. Let us assume (cf figure 27) that the ESF in the real case is proportional over $C_{max}^{rank\text{-}3} \in \left[\frac{1}{2}, 1\right]$ to $\left(2 - 2C_{max}^{rank\text{-}3}\right)^{\frac{7}{4}}$ and in the complex case to the square of this. Then, we have that the contributions over this half-domain to the Hilbert–Schmidt real and complex separability probabilities, respectively, are $\frac{2^6\cdot 7\cdot 1249}{3^6\cdot 5\cdot 13\cdot 31} \approx 0.380\,924$ (multiplied by a normalization constant approximately 0.177 365) and $\frac{13\cdot 289\,014\,610\,051}{2^9\cdot 3^9\cdot 5\cdot 11\cdot 23\cdot 29\cdot 31} \approx 0.327\,832$ (multiplied by a normalization constant approximately 0.086 232).

8.6. Rank-5 complex qubit–qutrit case

For the full-rank qubit–qutrit case, the counterpart—although not enjoying all the properties—of the two-qubit maximal concurrence formula (1) is [24, p 16]

$$C_{max}^{rank\text{-}6} = \max(0, \lambda_1 - \lambda_5 - 2\sqrt{\lambda_4\lambda_6}), \qquad (\lambda_1 \geqslant \lambda_2 \geqslant \lambda_3 \geqslant \lambda_4 \geqslant \lambda_5 \geqslant \lambda_6), \tag{23}$$

which, obviously (since $\lambda_6 = 0$), degenerates (using the same eigenvalue-ordering) to

$$C_{max}^{rank\text{-}5} = \lambda_1 - \lambda_5. \tag{24}$$

In figure 30—again under the hypothesis (ansatz) that the corresponding eigenvalue-parameterized-separability function is a (univariate) function of the maximal concurrence expression (24)—we show the analogue of figure 26 for the minimally degenerate (rank-5) generic real and complex qubit–qutrit case. (Again, in the complex case, we used the $SU(6)$-Euler-angle parameterization of Cacciatori [8, appendix A], while we used a yet unpublished Euler-angle parameterization of his of $SO(6)$ for the real case.) There are evident jumps in the real (blue) curve at $C_{max}^{rank\text{-}5} = \frac{1}{3}$ and $\frac{1}{2}$. (The still erratic nature of the complex (red) curve—we

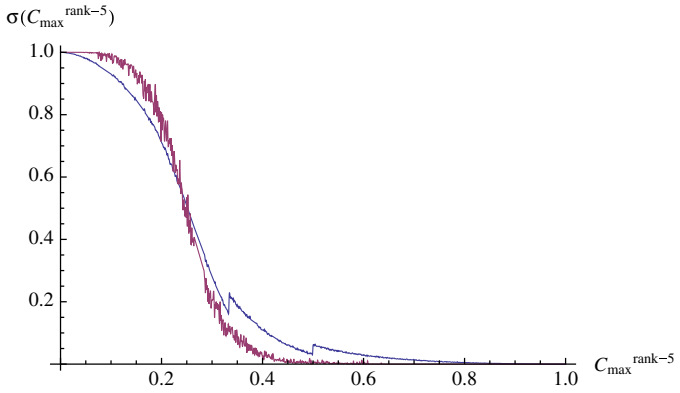

Figure 30. Qubit–qutrit eigenvalue-parameterized separability functions as a function of maximal concurrence for the generic rank-5 real and complex 6×6 density matrices. 104 200 TF-points were used in the real case and 181 600 in the complex case, while, for each such point, the interval $[0, 1]$ was sampled at 1000 equally spaced locations of $C_{\max}^{\text{rank-5}}$. The complex (red) curve is initially dominant. There are manifest discontinuities (jumps) at $C_{\max}^{\text{rank-5}} = \frac{1}{3}$ and $\frac{1}{2}$ in the real case.

used 1000 (not 500) equally spaced points in $[0, 1]$—makes it, at this point of sampling, difficult to gauge the applicability of the Dyson indices.) To test the applicability of the rank-5 version of the univariance hypothesis (14), we estimated the real and complex rank-5 qubit–qutrit Hilbert–Schmidt separability probabilities using the ESFs displayed in figure 30. The values we obtained were 0.097 232 and 0.022 6654, respectively, while the corresponding conjectures were—again somewhat disappointingly different—$\frac{16}{213} \approx 0.075\,1174$ and $\frac{16}{1199} \approx 0.013\,3445$.

8.7. Full-rank real and complex qubit–qutrit cases

In the two-qubit case, we had evolved a computational strategy in which we used the Mathematica command FindInstance to systematically generate random sets of three or four eigenvalues that yielded values of the maximal concurrence ((1) or (19)) at *equally spaced* intervals $C_{\max} \in [0, 1]$—and, similarly, in the rank-5 qubit–qutrit case (24). However, due to greater complexity in the rank-6 case, this strategy did not prove at all feasible for generating random sets of *six* eigenvalues yielding equally spaced values of the maximal concurrence (23).

So, we altered our approach, now simply randomly generating density matrices (again using the same quasi-Monte Carlo routines [20]) and recording their associated values of concurrence. We 'binned' these concurrence values into intervals of length $\frac{1}{50}$, and averaged the total measures recorded by the number of observations within the individual bins. We interpolated these average values to obtain the associated eigenvalue-parameterized separability functions (ESFs). We have generated the corresponding curves for both the full-rank real and complex generic qubit–qutrit cases, but they are still somewhat crude/rough in character. Nevertheless, we plot in figure 31(cf figures 23 and 27) normalized forms of the complex (red) curve and the *square* of the real (blue) curve. They appear to indicate possible adherence to the Dyson-index ansatz, since the two curves closely 'track' each other, at least (as our generally observed pattern in the two-qubit case would suggest) for the *higher* values of $C_{\max}^{\text{rank-6}}$. (It seems that this domain of possibly strict Dyson-index behavior may be $C_{\max}^{\text{rank-6}} \in \left[\frac{1}{3}, 1\right]$, while in the full-rank two-qubit case (figure 23), it highly convincingly appeared to be $C_{\max}^{\text{rank-4}} \in \left[\frac{1}{2}, 1\right]$. Our level of binning is perhaps too coarse for the detection of

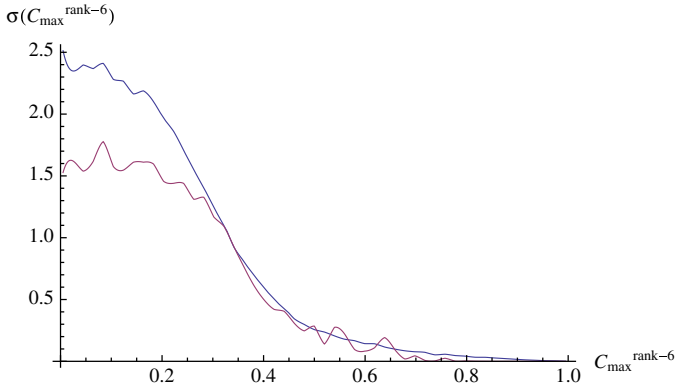

Figure 31. Joint plot (cf figure 23)—to test Dyson-index ansatz—of numerical estimates of the real $(\frac{\sigma^1(C_{\max}^{\text{rank-6}})}{\sigma^1(\frac{1}{3})})^2$ and complex $\frac{\sigma^2(C_{\max}^{\text{rank-6}})}{\sigma^2(\frac{1}{3})}$. (The complex (red) curve is lower at $C_{\max}^{\text{rank-6}} = 0$.) There were 62 086 051 20-dimensional TF-points (each point corresponding to a single density matrix) used in the real case and 451 373 489 35-dimensional TF-points in the complex case. Each of these points was allocated to one of fifty bins in the interval $C_{\max}^{\text{rank-6}} \in [0, 1]$.

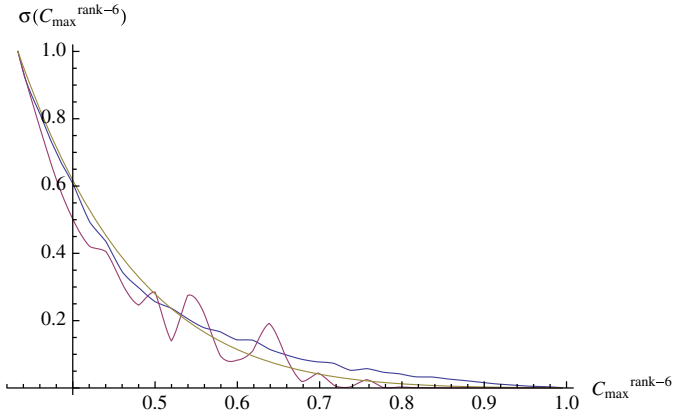

Figure 32. Same plot as in figure 31, but restricted to $C_{\max}^{\text{rank-6}} \in [\frac{1}{3}, 1]$, along with the insertion of the smooth, interweaving function $(\frac{4}{3} - C_{\max}^{\text{rank-6}})^7$.

possible discontinuities in the two curves.) We were interested in seeing how close the plotted curves came—under the rank-6 qubit–qutrit version of the univariance hypothesis (14)—to yielding the conjectured HS real and complex separability probabilities of $\frac{32}{213}$ and $\frac{32}{1199}$ [7, section X], but the requisite numerical integrations proved quite problematical to perform. In figure 32 we plot the two functions in figure 31 over the interval $\left[\frac{1}{3}, 1\right]$, along with the interweaving curve $\left(\frac{4}{3} - C_{\max}^{\text{rank-6}}\right)^7$.

9. Separability probability decompositions over $C_{\max}$ regions

9.1. $C_{\max} = 0$ *domain*

One can—in an apparently natural manner—consider the two-qubit real, complex and quaternionic Hilbert–Schmidt separability probabilities to be the sum of *three* components:

(1) the Hilbert–Schmidt *absolute* separability probabilities (corresponding to $C_{\max} = 0$); (2) the probabilities over the range $C_{\max} \in \left(0, \frac{1}{2}\right]$ and (3) the probabilities over the range $C_{\max} \in \left[\frac{1}{2}, 1\right]$. (For a contour plot of the 3-dimensional body $C_{\max} = 0$, see [8, figure 2].) Now, we have previously been able to compute the absolutely separable components [8, equations (34), (35)]. These are

$$P^{HS_{\text{real}}}_{C_{\max}=0} = \frac{6928 - 2205\pi}{2^{\frac{9}{2}}} \approx 0.034\,8338, \tag{25}$$

$$P^{HS_{\text{complex}}}_{C_{\max}=0} = \frac{\psi_1 - \psi_2\sqrt{2} - \psi_3\sqrt{2}\pi + \psi_4\sqrt{2}\sec^{-1}(3)}{2^{16}3^5} \approx 0.003\,658\,263\,054\,3035 \tag{26}$$

(the Bures (minimal monotone) metric analogue being considerably smaller, 0.000 161 792 [8, p 25]) where

$$\psi_1 = 956\,877\,309\,536,\ \psi_2 = 781\,862\,943\,168,$$

$$\psi_3 = 746\,624\,752\,335,\ \psi_4 = 1990\,999\,339\,560,$$

and

$$P^{HS_{\text{quat}}}_{C_{\max}=0} = -\frac{13(\phi_1 + \phi_2\sqrt{2} + \phi_3\sqrt{2}\pi - \phi_4\sqrt{2}\sec^{-1}(3))}{2^{34}\cdot 3^{11}} \approx 0.000\,039\,8703, \tag{27}$$

where

$$\begin{aligned}&\phi_1 = -806\,338\,156\,306\,739\,134\,839\,776, \quad \phi_2 = 658\,857\,590\,468\,226\,345\,222\,144,\\ &\phi_3 = 629\,162\,653\,900\,414\,735\,065\,195, \quad \phi_4 = 1677\,767\,077\,067\,772\,626\,840\,520.\end{aligned} \tag{28}$$

(These are 'conjecture-free' results, not dependent on any Dyson-index ansatz. In [8, equations (36), (37)] we gave a considerably lengthier, but fully equivalent, expression for $P^{HS_{\text{quat}}}_{C_{\max}=0}$. One might seek to find explanations for the large integers displayed above in terms of gamma functions. The computational challenges to computing analogous absolute separability results for the qubit–qutrit states appear to be highly formidable.)

9.2. $C_{\max} \in \left[\frac{1}{2}, 1\right]$

Further, accepting the strongly-supported Dyson-index ansatz (figure 25 and (18)) that $\sigma^{(1)}(C_{\max}(\lambda_1, \ldots, \lambda_4)) = \frac{(2-2C_{\max})^{\frac{3}{2}}}{\sqrt{30}}$ and $\sigma^{(2)}(C_{\max}(\lambda_1, \ldots, \lambda_4)) = \frac{(2-2C_{\max})^3}{15}$ for $C_{\max} \in \left[\frac{1}{2}, 1\right]$, we can now add to the absolute separability probabilities ($C_{\max} = 0$) listed immediately above, the conjectured probability contributions:

$$P^{HS_{\text{real}}}_{C_{\max}\in[\frac{1}{2},1]} = \frac{\sqrt{\frac{3}{10}}(3162\,214 - 738\,885\sqrt{2}\tan^{-1}(\sqrt{2}))}{2^{12}\cdot 5\cdot 7\cdot 17\cdot 19} \approx 0.025\,596\,477\,78, \tag{29}$$

and

$$P^{HS_{\text{complex}}}_{C_{\max}\in[\frac{1}{2},1]} = \frac{7\left(148\,453\,588\,142 - 79\,729\,806\,357\sqrt{2}\cot^{-1}\left(\frac{5}{\sqrt{2}}\right)\right)}{2^{31}\cdot 3^7\cdot 17} \approx 0.010\,290\,595\,19. \tag{30}$$

Further, using the Dyson-index ansatz with $\beta = 4$, we obtain

$$P^{HS_{\text{quat}}}_{C_{\max}\in[\frac{1}{2},1]} = \frac{5\left(\zeta_1 - \zeta_2\sqrt{2}\cot^{-1}\left(\frac{5}{\sqrt{2}}\right)\right)}{2^{66}\cdot 3^8\cdot 11\cdot 29\cdot 31}\kappa \approx 0.165\,191\kappa, \tag{31}$$

where

$$\zeta_1 = 174\,916\,374\,035\,295\,022\,487\,516\,506, \quad \zeta_2 = 42\,964\,561\,240\,209\,557\,008\,032\,951, \tag{32}$$

and κ is the $\beta = 4$ unknown and yet-unconjectured analogue of the presumed real and complex constants $\frac{1}{\sqrt{30}}$ and $\frac{1}{15}$. (In computing (29)–(32), we found a joint transformation of the form $\alpha_1 = \sqrt{\frac{\lambda_2}{\lambda_4}}$ and $\alpha_2 = \sqrt{\lambda_2 \lambda_4}$ to be helpful.)

9.2.1. Corollaries to the 'twofold' SBZ theorem. Since the probability is zero that a generic minimally degenerate two-qubit state is absolutely separable $\left(\text{that is, } P^{\text{rank-3}} = P^{\text{rank-3}}_{C_{\max} \in [0,1]}\right)$—as can be immediately deduced from (24)—we have simple corollaries to the twofold-theorem of Szarek, Bengtsson and Życzkowski [36] of the form

$$\frac{P^{\text{rank-4}}_{C_{\max} \in [0,1]}}{P^{\text{rank-3}}_{C_{\max} \in [0,1]}} = 2 - \frac{P^{\text{rank-4}}_{C_{\max}=0}}{P^{\text{rank-3}}_{C_{\max} \in [0,1]}} = 2 - \frac{P^{\text{rank-4}}_{C_{\max}=0}}{P^{\text{rank-3}}}, \tag{33}$$

where the Ps are Hilbert–Schmidt separability probabilities, for the real, complex or quaternionic two-qubit states.

9.3. $C_{\max} \in \left(0, \frac{1}{2}\right]$

So, the most conspicuous missing parts in the Hilbert–Schmidt separability probability 'puzzle' appear to us to be formulas for $P^{HS_{\text{real}}}_{C_{\max} \in (0, \frac{1}{2}]}$, $P^{HS_{\text{complex}}}_{C_{\max} \in (0, \frac{1}{2}]}$ and $P^{HS_{\text{quat}}}_{C_{\max} \in (0, \frac{1}{2}]}$. Of course, we can subtract the sums of the other two parts $\left(P^{HS_{\text{real}}}_{C_{\max}=0} + P^{HS_{\text{real}}}_{C_{\max} \in [\frac{1}{2}, 1]}, P^{HS_{\text{complex}}}_{C_{\max}=0} + P^{HS_{\text{complex}}}_{C_{\max} \in [\frac{1}{2}, 1]}\right.$ and $\left. P^{HS_{\text{quat}}}_{C_{\max}=0} + P^{HS_{\text{quat}}}_{C_{\max} \in [\frac{1}{2}, 1]}\right)$ from our overall conjectures of $\frac{8}{17}$, $\frac{8}{33}$ and $\frac{72\,442\,944}{936\,239\,725}$ to obtain 'induced' conjectures about these third components.

Since it now appears crucial to, additionally, model the eigenvalue-parameterized separability functions over the domain $C_{\max} \in \left(0, \frac{1}{2}\right]$, we present in figure 33, for the convenience of the interested reader, the previously generated [17, figure 1] estimates of these functions. The real (blue) curve is close to linear ($\approx 1 - 1.75 C_{\max}$). Also, we have noted that the complex (red) curve is quite well fitted by $\cos^{22}(C_{\max})$ and $\cos^5(2C_{\max})$. However, we appear here to lack a strictly similar Dyson-index ansatz to serve as a guide in constructing these two functions (cf [7]). Also, there were indications given in [17, figures 3–5] that these two functions have multiple (matching) points of discontinuity in $C_{\max} \in \left(0, \frac{1}{2}\right]$. (These were $C_{\max} \approx 0.204, 0.294, 0.34$.) The lack of a Dyson-index pattern strictly similar to that found apparently for $C_{\max} \in \left[\frac{1}{2}, 1\right]$ to exploit for $C_{\max} \in \left(0, \frac{1}{2}\right]$ is immediately apparent from figure 34. A *flat* line over at least some subdomain of $C_{\max} \in \left(0, \frac{1}{2}\right]$ would indicate such a Dyson-index pattern. Clearly, no such flatness appears there. However, it now seems that there is a pattern of the approximate form:

$$\sigma^2\left(C^{\text{rank-4}}_{\max}\right) = \left(\sqrt{1 + 2C^{\text{rank-4}}_{\max}}\,\sigma^1\left(C^{\text{rank-4}}_{\max}\right)\right)^2, C^{\text{rank-4}}_{\max} \in \left(0, \tfrac{1}{2}\right]. \tag{34}$$

(We have already noted that $\sigma^1\left(C^{\text{rank-4}}_{\max}\right) \approx 1 - 1.75 C^{\text{rank-4}}_{\max}$ in this half-domain.) The highly interesting nature of figure 34 led us to similarly re-examine the minimally degenerate rank-3 two-qubit scenarios (figure 26). Thus, we obtained figure 35. Now $1 + 3C_{\max}$ serves as an excellent linear approximation, and we have a relation analogous to (34):

$$\sigma^2\left(C^{\text{rank-3}}_{\max}\right) = \left(\sqrt{1 + 3C^{\text{rank-3}}_{\max}}\,\sigma^1\left(C^{\text{rank-3}}_{\max}\right)\right)^2, C^{\text{rank-3}}_{\max} \in \left(0, \tfrac{1}{2}\right]. \tag{35}$$

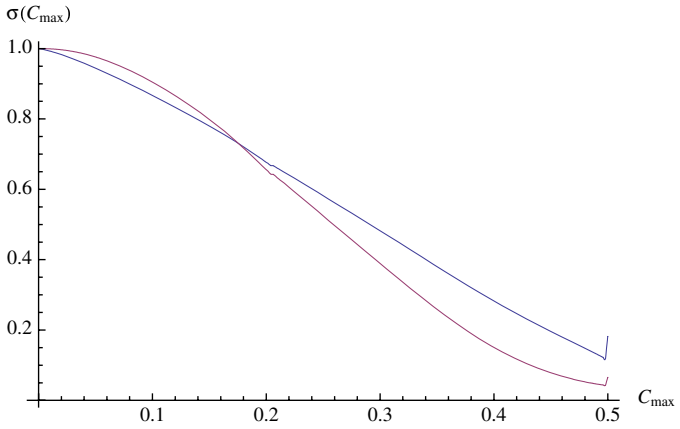

Figure 33. Previously generated [17, figure 1] estimates of the two-qubit real and complex eigenvalue-parameterized separability functions over the domain $C_{\max} \in (0, \frac{1}{2}]$. The complex (red) curve is initially higher-valued and the real (blue) curve, close to linear.

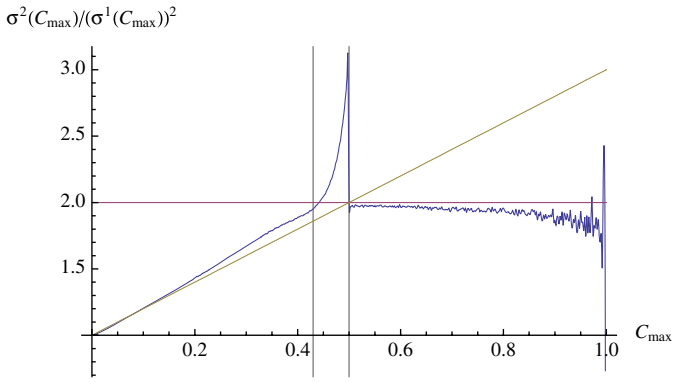

Figure 34. Estimated ratio (for the full-rank two-qubit case) of $\frac{\sigma^2(C_{\max}^{\text{rank-4}})}{(\sigma^1(C_{\max}^{\text{rank-4}}))^2}$ along with the approximating lines $1 + 2C_{\max}$ and 2 the vertical lines $C_{\max} = \frac{43}{100}$ and $\frac{1}{2}$.

If we plot $\frac{\sigma^2(C_{\max}^{\text{rank-4}})}{1+2C_{\max}^{\text{rank-4}}}$ *versus* $\left(\sigma^1\left(C_{\max}^{\text{rank-4}}\right)\right)^2$ and also $\frac{\sigma^2(C_{\max}^{\text{rank-3}})}{1+3C_{\max}^{\text{rank-3}}}$ *versus* $\left(\sigma^1\left(C_{\max}^{\text{rank-3}}\right)\right)^2$ over the half-domain, the two curves within each set are essentially indistinguishable. We have investigated analogous plots of the same form for the minimally degenerate qubit–qutrit (figure 30) and full-rank (figure 31) cases over $C_{\max} \in \left[0, \frac{1}{3}\right]$. They are much rougher in nature, due to our limited sampling, but still indicate initial monotonically increasing (non-flat) behavior over $C_{\max}$.

9.4. Total probabilities over C_{max} regions

Let us also point out that the Hilbert–Schmidt probability ($\tilde{P}$) that a generic two-qubit real state (separable *or* entangled) lies in the domain $C_{\max} \in \left[\frac{1}{2}, 1\right]$ is

$$\tilde{P}^{HS_{\text{real}}}_{C_{\max} \in [\frac{1}{2}, 1]} = \frac{75\,962 - 25\,515\sqrt{2}\tan^{-1}(\sqrt{2})}{2^{13} \cdot 3^3} \approx 0.187\,584, \tag{36}$$

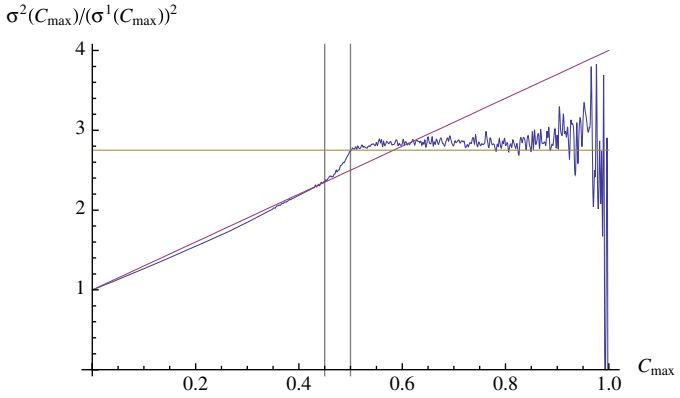

Figure 35. Estimated ratio (for the minimally degenerate rank-3 two-qubit case) of $\frac{\sigma^2(C_{\max}^{\text{rank}=3})}{(\sigma^1(C_{\max}^{\text{rank}=3}))^2}$ along with the approximating lines $1+3C_{\max}$ and $\frac{11}{4}$ and the vertical lines $C_{\max}=\frac{9}{20}$ and $\frac{1}{2}$.

with the complex counterpart being

$$\tilde{P}^{HS_{\text{complex}}}_{C_{\max}\in[\frac{1}{2},1]} = \frac{174\,957\,361\,466 - 124\,912\,178\,055\sqrt{2}\cot^{-1}\left(\frac{5}{\sqrt{2}}\right)}{2^{31}\cdot 3^5} \approx 0.241\,961, \tag{37}$$

and the quaternionic analogue being

$$\tilde{P}^{HS_{\text{quat}}}_{C_{\max}\in[\frac{1}{2},1]} = \frac{\gamma_1 - \gamma_2\sqrt{2}\cot^{-1}\left(\frac{5}{\sqrt{2}}\right)}{2^{63}\cdot 3^{10}} \approx 0.323\,053, \tag{38}$$

where

$$\gamma_1 = 217\,894\,901\,318\,574\,565\,900\,294, \qquad \gamma_2 = 107\,614\,737\,772\,623\,370\,233\,945. \tag{39}$$

(The comparable total probabilities for the minimally degenerate two-qubit states have been given in section 8.5.1.) Since for the absolutely separable states ($C_{\max}=0$), the two probabilities $P_{C_{\max}=0}$ and $\tilde{P}_{C_{\max}=0}$ are equivalent, we can immediately determine (by subtracting from 1 our known HS probabilities $P_{C_{\max}=0}$ and $\tilde{P}_{C_{\max}\in[\frac{1}{2},1]}$) the *complementary* probabilities, $\tilde{P}_{C_{\max}\in(0,\frac{1}{2}]}$. Numerically, these are $\tilde{P}^{HS_{\text{real}}}_{C_{\max}\in(0,\frac{1}{2}]} \approx 0.777\,582$, $\tilde{P}^{HS_{\text{complex}}}_{C_{\max}\in(0,\frac{1}{2}]} \approx 0.754\,381$ and $\tilde{P}^{HS_{\text{quat}}}_{C_{\max}\in(0,\frac{1}{2}]} \approx 0.676\,907$.

10. Concluding remarks

Our analyses of two-qubit *diagonal-entry*-parameterized separability functions (DESFs) [7, 31, 45] and *eigenvalue*-parameterized separability functions (ESFs) [8, 17] completely share a *common* goal: the determination of two-qubit separability volumes and probabilities (in terms of various metrics). As pieces of these formidable objectives begin to be assembled, we can pose a further challenge—to find transformations between the two *different* sets of coordinates used—that is, (1) the *diagonal entries* and (2) the *eigenvalues* of 4×4 density matrices—that will map one set of separability functions into the other. The Schur–Horn theorem, which asserts that the decreasingly ordered vector of eigenvalues of an Hermitian matrix *majorizes* the decreasingly ordered vector of its diagonal entries [46, chapter 4] (cf [47, 48]), would appear to be of possible relevance in this regard, particularly since

the maximal concurrence $C_{\max}$ over spectral orbits (12) is expressed in terms of the *ordered* eigenvalues.

In terms of the diagonal entries $(D_1, D_2, D_3, D_4 = 1 - D_1 - D_2 - D_3)$ of 4×4 two-qubit density matrices, we can express the conjectured Hilbert–Schmidt separability probability [7], $\frac{8}{33}$, of generic complex states in the form

$$\frac{8}{33} = \frac{12\,108\,096\,000}{71} \int\int\int (D_1 D_2 D_3 D_4)^3 (3-\nu)^2 \nu \, \mathrm{d}D_1 \, \mathrm{d}D_2 \, \mathrm{d}D_3, \tag{40}$$

where $\nu \equiv \frac{D_1 D_4}{D_2 D_3}$, and the integration extends over the unit simplex, but with the restriction $\nu \leqslant 1$. (We note that $12\,108\,096\,000 = 2^9 \cdot 3^3 \cdot 5^3 \cdot 7^2 \cdot 11 \cdot 13$. Let us also observe that the variable $\log \nu$ conveniently ranges over the entire real axis and is symmetric about the origin.)

Additionally, in terms of the eigenvalues $(\lambda_1, \lambda_2, \lambda_3, 1 - \lambda_1 - \lambda_2 - \lambda_3)$ of 4×4 two-qubit density matrices, we can express this *same* separability probability as (cf (14))

$$\frac{8}{33} = 2201\,472\,000 \int\int\int \sigma^{(2)}(C_{\max}(\lambda_1, \ldots, \lambda_4)) \Pi_{i<j}^4 (\lambda_i - \lambda_j)^2 \, \mathrm{d}\lambda_1 \, \mathrm{d}\lambda_2 \, \mathrm{d}\lambda_3, \tag{41}$$

and the integration extends over that part (Weyl chamber [16]) of the unit simplex for which $\lambda_1 \geqslant \lambda_2 \geqslant \lambda_3 \geqslant \lambda_4$. (We note that, interestingly, in light of the just previous factorization, $2201\,472\,000 = 2^{10} \cdot 3^3 \cdot 5^3 \cdot 7^2 \cdot 13$.) Here $\sigma^{(2)}(C_{\max}(\lambda_1, \ldots, \lambda_4))$ is the (two-qubit complex ($\beta = 2$)) eigenvalue-parameterized separability function that we have previously sought to determine [17, figure 1], and was found to be very well fitted by $\frac{(2-2C_{\max})^3}{15}$ for $C_{\max} \in \left[\frac{1}{2}, 1\right]$ (figure 25 and (18)). (It is possible to reexpress these two last integrals so that *both* are taken over the *same* complete 3-dimensional unit simplex.) Further still, our generic complex two-qubit *Bures* separability probability conjecture (2) [4, table VI] takes the form

$$\frac{1680(\sqrt{2}-1)}{\pi^8} = \frac{\pi^2}{71\,680} \int\int\int \frac{\sigma^{(2)}(C_{\max}(\lambda_1 \ldots \lambda_4))}{\sqrt{\lambda_1 \lambda_2 \lambda_3 \lambda_4}} \Pi_{i<j}^4 \frac{(\lambda_i - \lambda_j)^2}{\lambda_i + \lambda_j} \, \mathrm{d}\lambda_1 \, \mathrm{d}\lambda_2 \, \mathrm{d}\lambda_3. \tag{42}$$

It is abundantly clear: (a) that this (piecewise continuous) function $\sigma^{(2)}(C_{\max}(\lambda_1, \ldots, \lambda_4))$ has a jump discontinuity at $C_{\max} = \frac{1}{2}$ (as well as does its real counterpart $\sigma^{(1)}(C_{\max}(\lambda_1 \ldots \lambda_4))$ and (b) that in the diagonal-entry-parameterized scenario, the value $\nu = \frac{D_1 D_4}{D_2 D_3} = 1$ is a locus of special symmetry. In this regard, we might speculate that if one can find a coordinate transformation between the two separability probability expressions ((40) and (41)), then those values of the λ_i's for which $C_{\max} = \frac{1}{2}$ will be mapped to those values of the D_i's for which $\nu = 1$.

Through the use of the jacobian transformation of the diagonal entry D_3 (say) to ν [45, equation (11)], and subsequent integration over D_1 and D_2, it is possible to explicitly reduce the computation of the trivariate integral (40) to that of a univariate integral in ν. In figure 36, we show—based on numerical calculations—the univariate marginal probability distributions of the Hilbert–Schmidt measure over the real and complex two-qubit states in terms of $C_{\max}^{\text{rank-4}}$ (cf (20)–(22)). Similarly, to their rank-3 counterparts (figure 28), these curves have differently positioned peaks and are not symmetric, but skewed to the right. (We take the range of $C_{\max}^{\text{rank-4}}$ to be $\left[-\frac{1}{2}, 1\right]$, to accord with actual values, rather than the conventional [0, 1] (cf (12)).) In figure 37, we show the Bures-metric counterpart, although we encounter some 'glitch' in displaying the real curve here.

The counterparts to formulas (40) and (41), in light of our conjecture [7] that the Hilbert–Schmidt separability probability of the generic *real* two-qubit states is $\frac{8}{17}$, are (the domains of integration being the same)

$$\frac{8}{17} = \frac{1209\,600}{17} \int\int\int (D_1 D_2 D_3 D_4)^{3/2} (3-\nu) \sqrt{\nu} \, \mathrm{d}D_1 \, \mathrm{d}D_2 \, \mathrm{d}D_3, \tag{43}$$

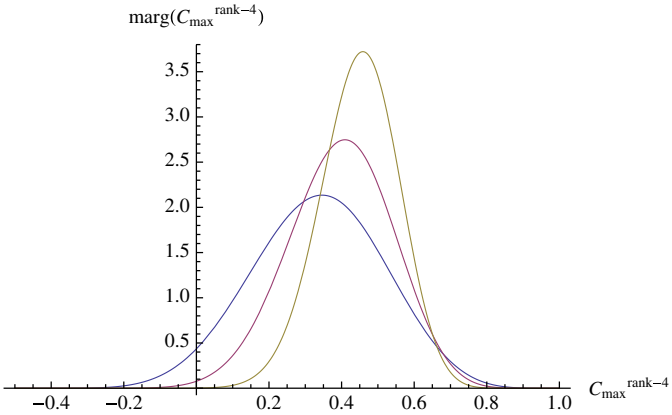

Figure 36. Full-rank two-qubit univariate marginal probability distributions over $C_{\max}^{\text{rank-4}} \in [-\frac{1}{2}, 1]$ of the 3-dimensional Hilbert–Schmidt measures on the eigenvalues. The quaternionic curve has the highest peak, and the real curve, the lowest. Numerical methods were used.

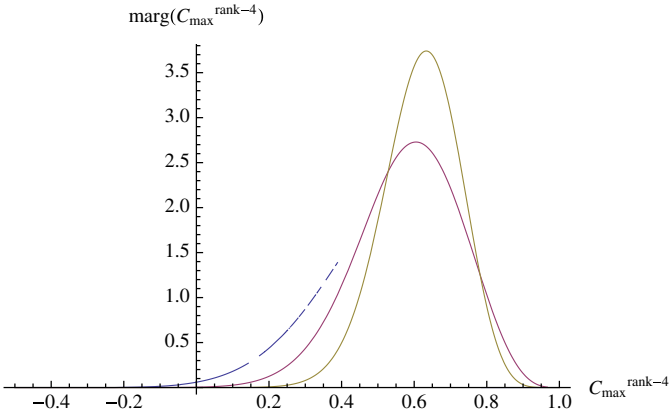

Figure 37. Counterpart to figure 36 based on the Bures metric. The quaternionic curve has the highest peak, followed by the complex curve, with the (incompletely constructed) real curve, apparently the lowest. Numerical methods were used.

and

$$\frac{8}{17} = \frac{15\,482\,880}{17} \int\int\int \sigma^{(1)}(C_{\max}(\lambda_1 \ldots \lambda_4)) \Pi_{i<j}^{4} (\lambda_i - \lambda_j)\, \mathrm{d}\lambda_1\, \mathrm{d}\lambda_2\, \mathrm{d}\lambda_3. \tag{44}$$

(Here, $1209\,600 = 2^8 \cdot 3^3 \cdot 5^2 \cdot 7$ and $15\,482\,880 = 2^{14} \cdot 3^3 \cdot 5 \cdot 7$. It appears (figure 27 and (18)) that possibly $\sigma^{(1)}(C_{\max}(\lambda_1 \ldots \lambda_4)) = \frac{(2-2C_{\max})^{\frac{3}{2}}}{\sqrt{30}}$ for $C_{\max} \in \left[\frac{1}{2}, 1\right]$.)

Let us point out the possible relevance of the concept of the *Thouless energy* [49, p 734] in the modeling of the threshold or crossover effect we have numerically observed for eigenvalue-parameterized separability functions in both the full generic real and complex two-qubit and qubit–qutrit cases. There, the Dyson indices ($\beta = 1, 2$) of random matrix theory only seemed to apply above a certain value of the maximal concurrence $C_{\max}$ (that is,

$\frac{1}{2}$ in the two-qubit case, and possibly $\frac{1}{3}$ in the qubit–qutrit instance). (It remains to formally reconcile these observations with the ones that, in terms of diagonal-entry-parameterized separability functions, Dyson-index behavior appear to be *strictly* followed [7].)

Acknowledgments

I would like to express appreciation to the Kavli Institute for Theoretical Physics (KITP) for computational support in this research, as well as to K Życzkowski for his interest and for a number of suggestions concerning the analyses and their presentation.

References

[1] Życzkowski K, Horodecki P, Sanpera A and Lewenstein M 1998 *Phys. Rev.* A **58** 883
[2] Slater P B 1999 *J. Phys. A: Math. Gen.* **32** 5261
[3] Slater P B 2000 *Euro. Phys. J.* B **17** 471
[4] Slater P B 2005 *J. Geom. Phys.* **53** 74
[5] Slater P B 2005 *Phys. Rev.* A **71** 052319
[6] Slater P B 2006 *J. Phys. A: Math. Gen.* **39** 913
[7] Slater P B 2007 *J. Phys. A: Math. Theor.* **40** 14279
[8] Slater P B 2009 *J. Geom. Phys.* **59** 17
[9] Ioannou L M 2007 *Quantum Inform. Comput.* **7** 335
[10] Ye D 2009 arXiv:0902.1505
[11] Appel K and Haken W 1977 *Ill. J. Math.* **21** 439
[12] Soifer A 2009 *The Mathematical Coloring Book* (New York: Springer)
[13] Życzkowski K and Sommers H-J 2003 *J. Phys. A: Math. Gen.* **36** 10115
[14] Sommers H-J and Życzkowski K 2003 *J. Phys. A: Math. Gen.* **36** 10083
[15] Andai A 2006 *J. Phys. A: Math. Gen.* **39** 13641
[16] Bengtsson I and Życzkowski K 2006 *Geometry of Quantum States* (Cambridge: Cambridge University Press)
[17] Slater P B 2008 *J. Phys. A: Math. Theor.* **41** 505303
[18] Byrd T, Tilma M and Sudarshan E C G 2002 *J. Phys. A: Math. Gen.* **35** 10445
[19] Faure H and Tezuka S 2002 *Monte Carlo and Quasi-Monte Carlo Methods 2000 (Hong Kong)* ed K T Tang, F J Hickernell and H Niederreiter (Berlin: Springer) p 242
[20] Ökten G 1999 *Math. Educ. Res.* **8** 52
[21] Tilma T and Sudarshan E C G 2002 *J. Phys. A: Math. Gen.* **35** 10467
[22] Wootters W K 1998 *Phys. Rev. Lett.* **80** 2245
[23] Iwai T 2007 *J. Phys. A: Math. Theor.* **40** 1361
[24] Hildebrand R 2007 *J. Math. Phys.* **48** 102108
[25] Ozawa M 2000 *Phys. Lett.* A **268** 158
[26] Petz D and Sudár C 1996 *J. Math. Phys.* **37** 2662
[27] Gibilisco P and Isola T 2003 *J. Math. Phys.* **44** 3752
[28] Petz D 1994 *J. Math. Phys.* **35** 780
[29] Krattenthaler C and Slater P B 2000 *IEEE Trans. Info. Theory* **46** 801
[30] Hayashi M 2008 arXiv:0806.1091
[31] Slater P B 2008 *J. Geom. Phys.* **58** 1101
[32] Peres A 1996 *Phys. Rev. Lett.* **77** 1413
[33] Horodecki M, Horodecki P and Horodecki R 1996 *Phys. Lett.* A **223** 1
[34] Horodecki R, Augusiak R and Demianowicz M 2008 *Phys. Rev.* **77** 030301
[35] Dehaene F, Verstraete J and Moor B D 2002 *J. Mod. Opt.* **49** 1277
[36] Bengtsson S, Szarek I and Życzkowski K 2006 *J. Phys. A: Math. Gen.* **39** L119
[37] Lesniewski A and Ruskai M B 1999 *J. Math. Phys.* **40** 5702
[38] Alicki R and Fannes M 2004 *Open Syst. Inform. Dyn.* **11** 339
[39] Abe S 2003 *Phys. Rev.* E **68** 031101
[40] Slater P B 2006 *J. Math. Phys.* **47** 022104
[41] Kogut J B, Stephanov M A, Toublan D, Verbaarschot J J M and Zhitnitsky A 2000 *Nucl. Phys.* B **582** 477
[42] Caselle M and Magnea U 2004 *Phys. Rep.* **394** 41
[43] Ishizaka S and Hiroshima T 2000 *Phys. Rev.* A **62** 022310

[44] Verstraete F, Audenaert K and DeMoor B 2001 *Phys. Rev.* A **64** 012316
[45] Slater P B 2007 *Phys. Rev.* A **75** 032326
[46] Horn R A and Johnson C R 1991 *Matrix Analysis* (New York: Cambridge University Press)
[47] Nielsen M A and Vidal G 2001 *Quantum Inform. Comput.* **1** 76
[48] Carlen E A 2009 arXiv:math.FA/0904.0734
[49] Beenakker C W J 1997 *Rev. Mod. Phys.* **69** 731